Differential regulation of cranial and cardiac neural crest by Serum Response Factor

Colin J. Dinsmore and Philippe Soriano*

Department of Cell, Development, and Regenerative Biology

Icahn School of Medicine at Mount Sinai

New York, NY 10029

*Corresponding author: philippe.soriano@mssm.edu

Keywords: SRF, MRTF, TCF, craniofacial development, neural crest, transcription

Abstract

Serum response factor (SRF) is an essential transcription factor that influences many cellular processes including cell proliferation, migration, and differentiation. SRF directly regulates and is required for immediate early gene (IEG) and actin cytoskeleton-related gene expression. SRF coordinates these competing transcription programs through discrete sets of cofactors, the Ternary Complex Factors (TCFs) and Myocardin Related Transcription Factors (MRTFs). The relative contribution of these two programs to *in vivo* SRF activity and mutant phenotypes is not fully understood. To study how SRF utilizes its cofactors during development, we generated a knock-in $Srf^{\alpha l}$ allele in mice harboring point mutations that disrupt SRF-MRTF-DNA complex formation but leave SRF-TCF activity unaffected. Homozygous $Srf^{\alpha l/\alpha l}$ mutants die at E10.5 with notable cardiovascular phenotypes, and neural crest conditional mutants succumb at birth to defects of the cardiac outflow tract but display none of the craniofacial phenotypes associated with complete loss of SRF in that lineage. Our studies further support an important role for MRTF mediating SRF function in cardiac neural crest and suggest new mechanisms by which SRF regulates transcription during development.

Introduction

Multicellular development requires the precise management of cellular behaviors including proliferation, migration, and differentiation. These are coordinated through intercellular communication pathways, such as growth factor signaling, that couple extracellular information with internal effectors, including transcription factors (TFs) (Fantauzzo & Soriano, 2015; Lemmon & Schlessinger, 2010). The balance between

opposing transcription programs is tuned by signaling pathways which activate specific TFs or in some cases cofactors that direct the behavior of a common TF. One example of the latter is the essential transcription factor Serum Response Factor (SRF) (Posern & Treisman, 2006). SRF is necessary for the expression of immediate early genes (IEGs) in cells stimulated with serum or growth factors, as well as many genes related to the actin cytoskeleton, contractility, and muscle differentiation.

SRF binds a conserved DNA regulatory sequence known as a CArG box, a motif found at many cytoskeletal and growth-factor inducible gene promoters (Mohun et al., 1991; Norman et al., 1988; Q. Sun et al., 2006). SRF can, however, effect at least two unique transcriptional programs by coupling with two families of cofactors that compete for a common binding site on SRF itself (Miano, 2003; Wang et al., 2004) (Figure 1A). The ternary complex factors (TCFs) are E26 transformation-specific (ETS) family proteins activated by extracellular signal-regulated kinase 1/2 (ERK1/2) phosphorylation (Mylona et al., 2016). Once activated, they bind DNA and promote cellular proliferation by transcribing IEGs in coordination with SRF (Esnault et al., 2017; Gualdrini et al., 2016). There are three TCF members in mouse and human: ELK1, ELK3/NET, and ELK4/SAP1 (Posern & Treisman, 2006). Opposing SRF-TCF activity are the Myocardin Related Transcription Factors (MRTFs). These cofactors rely on SRF to bind DNA, promote cytoskeletal gene expression, and are particularly important in muscle differentiation (Posern & Treisman, 2006). MRTFs bind to and are inhibited by G-actin. Polymerization of G-actin into F-actin liberates MRTFs to translocate to the nucleus and bind SRF (Miralles et al., 2003). This can be promoted by multiple signaling pathways, including

phosphoinositide 3-kinase (PI3K), that stimulate guanine nucleotide exchange factors to activate F-actin-promoting Rho-family GTPases (Brachmann et al., 2005; Hanna & El-Sibai, 2013; Jimenez et al., 2000; Vasudevan & Soriano, 2014). MRTFs are also positively and negatively regulated by extensive phosphorylation (Panayiotou et al., 2016). Three MRTFs are known to interact with SRF: Myocardin itself, MRTF-A/MKL1/MAL, and MRTF-B (Parmacek, 2007). *Mycod* is expressed specifically in muscle while *Mrtfa* and *Mrtfb* are more broadly expressed (Posern & Treisman, 2006). A fourth MRTF, MAMSTR/MASTR, interacts with MEF2 proteins and is not known to bind SRF (Creemers et al., 2006).

Srf and its cofactors have been extensively studied genetically. *Srf*$^{-/-}$ mutant mice die between E6.5 and E8.5 showing defects in mesoderm formation (Arsenian et al., 1998; Niu et al., 2005). Cofactor knockouts are comparatively mild. Single TCF mutants are all fully or partially viable (Ayadi et al., 2001; Cesari et al., 2004; Costello et al., 2004; Weinl et al., 2014) and *Elk1; Elk3; Elk4* triple null mice have not been described in detail but survive until E14.5 without obvious defects (Costello et al., 2010; Gualdrini et al., 2016). *Mrtfa*$^{-/-}$ mutant mice are viable (Li et al., 2006; Y. Sun et al., 2006) whereas *Mrtfb*$^{-/-}$ mice are inviable between E13.5-E15.5, exhibiting cardiovascular defects (Li et al., 2012; Oh et al., 2005). *Myocd*$^{-/-}$ mice have the most severe phenotype and die at E10.5, also from cardiovascular defects (Espinoza-Lewis & Wang, 2014; Li et al., 2003). *Mrtfa; Mrtfb* double null mice have not been described, but conditional double mutants have shown these factors exhibit redundancy and broadly phenocopy loss of *Srf* in several tissues and cell types (Cenik et al., 2016; Guo et al., 2018; S. Li et al., 2005; Trembley et al.,

2015). However, studies comparing *Srf* and *Mrtfa; Mrtfb* mutants are not always identical. In megakaryocytes, loss of *Mrtfa* and *Mrtfb* is more severe than loss of *Srf* and there are large gene expression differences in the two models (Smith et al., 2012). Indeed, there is evidence that MRTFs may regulate genes independent of SRF or act as cofactors for TFs other than SRF (Asparuhova et al., 2011; Kim et al., 2017). Whether the differences in *Srf* versus *Mrtfa; Mrtfb* loss-of-function studies are due to SRF-TCF activity, SRF-independent MRTF activity, or TCF/MRTF-independent SRF activity remains uncertain.

One tissue in which SRF was found to be essential is the neural crest (NC) (Newbern et al., 2008; Vasudevan & Soriano, 2014). The NC is a transient developmental population of cells that arises from the dorsal neural tube, migrates ventrally throughout the embryo, and gives rise to numerous cell types including the bone and connective tissue of the face, as well as smooth muscle cells in the cardiac outflow tract (Bronner & Simoes-Costa, 2016). The extensive migration, proliferation, and various differentiation outcomes these cells undergo requires accurate coordination, and decades of study have revealed a panoply of signaling pathways and transcription factors important in these processes, including the fibroblast growth factor (FGF) pathway, platelet-derived growth factor (PDGF) pathway, and SRF itself (Brewer et al., 2015; Dinsmore & Soriano, 2018; Newbern et al., 2008; Rogers & Nie, 2018; Tallquist & Soriano, 2003; Vasudevan & Soriano, 2014). We and others have previously shown that *Srf* is required in the NC for craniofacial and cardiovascular development (Newbern et al., 2008; Vasudevan & Soriano, 2014). Intriguingly, mice homozygous for a hypomorphic allele of *Mrtfb* die shortly after birth with cardiac outflow tract defects and can be rescued by a neural crest-

specific transgene (J. Li et al., 2005). Assays in mouse embryonic palatal mesenchyme cells (MEPMs) indicated that stimulation with the secreted ligands Fibroblast Growth Factor (FGF) or Platelet-Derived Growth Factor (PDGF) promoted SRF-TCF complex formation, but only PDGF promoted SRF-MRTF interactions, in a PI3K-dependent manner (Vasudevan & Soriano, 2014). Supporting the importance of SRF-MRTF interactions, *Srf* interacted genetically with *Pdgfra* but not *Fgfr1* in NC (Vasudevan & Soriano, 2014). However, the contributions of each SRF-cofactor transcriptional program to the overall *Srf* NC phenotype are unclear.

In this study, we further characterize the molecular consequences of losing *Srf* expression in the NC through marker analysis and expression profiling, finding the most highly-downregulated genes to be cytoskeletal in nature. We then test the presumed requirement of SRF-MRTF interactions using a novel $Srf^{\alpha l}$ allele carrying mutations that prevent SRF-MRTF-DNA ternary complex formation to circumvent MRTF redundancy and control for possible SRF-independent MRTF activity. These embryos have striking developmental defects that are outwardly similar to *Myocd* mutant mice. Conditional NC mutants reveal an essential role for optimal SRF-MRTF activity in the cardiac crest, whereas the mutation is well-tolerated in the cranial NC. These observations raise the possibility that non-cardiovascular tissue may be able to develop with only minimal SRF-MRTF activity or that SRF can support cytoskeletal gene expression on its own or with other cofactors.

Results

131 $Srf^{flox/flox}$; $Wnt1\text{-}Cre^{Tg/+}$ *mice develop a midfacial cleft and bleb, characterized by reduced*
132 *cytoskeletal gene expression.* To establish a phenotypic baseline for embryos lacking *Srf*
133 in NC, we first examined conditional null embryos at E11.5 and E12.5 and assessed their
134 morphology. Consistent with our previous study, a midfacial cleft develops from E10.5 to
135 E11.5, becoming prominent at E11.5 as a failure of the medial nasal process and lateral
136 nasal process (MNP and LNP, respectively) to converge at the midline (Figure 1B-C)
137 (Vasudevan & Soriano, 2014). By E12.5, a fluid-filled bleb develops at the midline, often
138 with hemorrhaging into the midfacial cavity (Figure 1B). Embryos turned necrotic starting
139 at E12.5 and did not survive past E13.5.

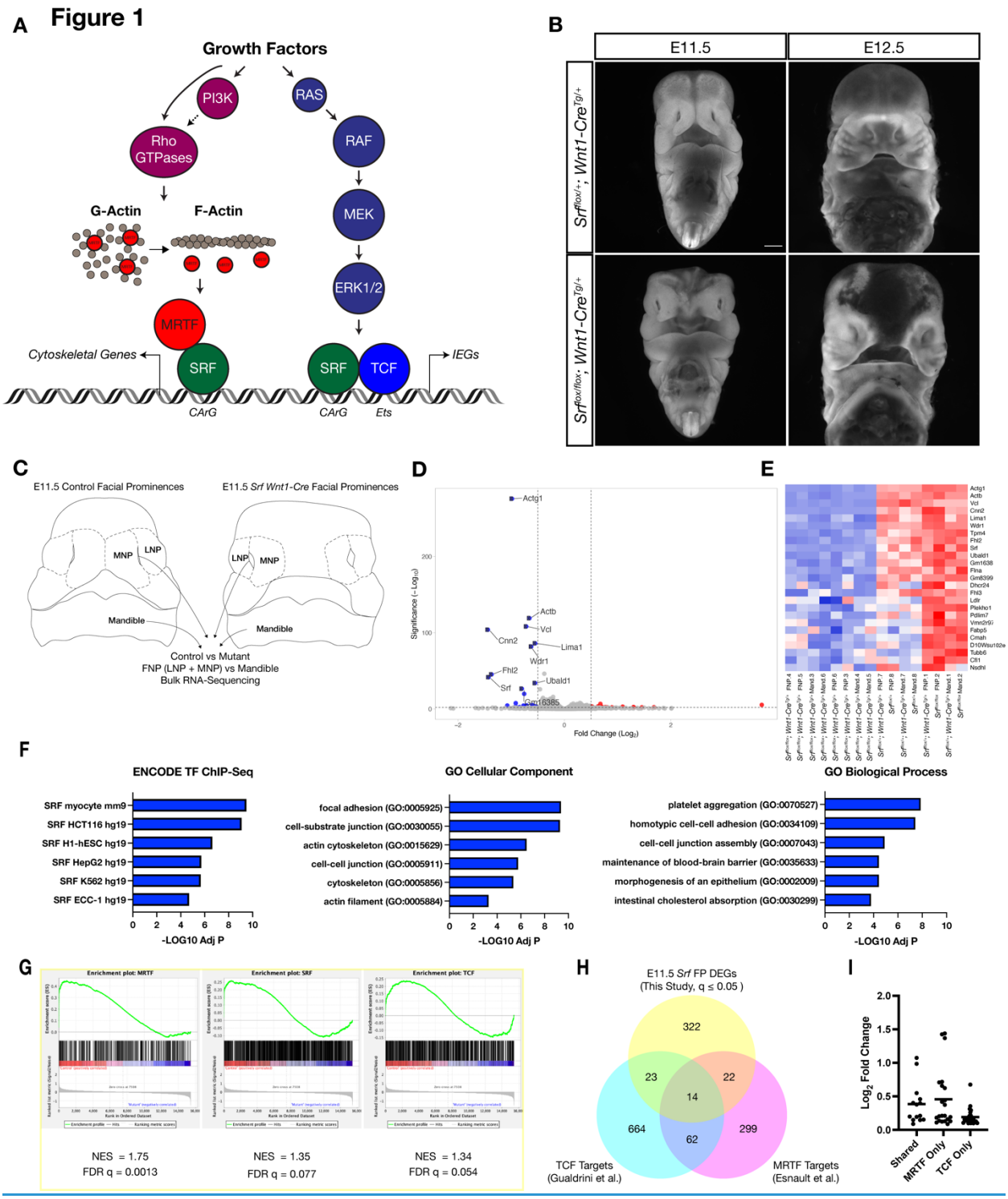

Figure 1
Loss of Srf *in NC affects cytoskeletal gene expression*
(A) Diagram depicting SRF, its TCF and MRTF cofactors, and the upstream signals that regulate them. (B) DAPI stained embryos at E11.5 and E12.5 show a facial cleft following loss of *Srf* in NC. Scale bar represents 1mm. (C) Diagram depicting RNA-sequencing strategy. (D) Volcano plot showing DEGs in *Srf* NC conditional mutants. Genes with a p value < 0.01 and $\log_2$ fold change (FC) > 0.25 are colored. Select genes are labeled. (E) A heatmap of the top 25 DEGs by q value. The samples cluster by genotype and are color-coded by Z-score. (F) Gene set enrichment analysis (GSEA) using a list of DEGs with q ≤ 0.05 and Log2FC ≤ -0.25. Enrichment for ENCODE TF ChIP-Seq, GO Cellular Component, and GO Biological Process are shown. (G) GSEA for known SRF, MRTF, and TCF ChIP targets from previous datasets (Esnault et al., 2014; Gualdrini et al., 2016) across our entire dataset. (H) Overlap of known MRTF and TCF targets with DEGs q ≤ 0.05. (I) Absolute value of $\log_2$ FC for DEGs that overlap with each category. Horizontal bar indicates the mean (0.385 Shared, 0.378 MRTF, 0.219 TCF).

We sought to better understand the molecular defects that underly this outcome. As *Srf* has been implicated in mediating cell differentiation, we asked whether early craniofacial patterning was affected. However, expression of the differentiation markers *Msx1* (craniofacial mesenchyme), *Alx3* (MNP and LNP mesenchyme, medial mandibular mesenchyme), and *Six3* (ventral forebrain, nasal placode, eye), as well as the markers of patterning centers *Shh* (ventral forebrain, weak oral MNP and mandibular epithelium), and *Fgf8* (ventral forebrain, oral MNP and epithelium) were all unaffected at E10.5 as assessed by *in situ* hybridization, suggesting craniofacial patterning was largely normal at this stage (Figure 1 Supplement 1).

Figure 1 Supplement 1

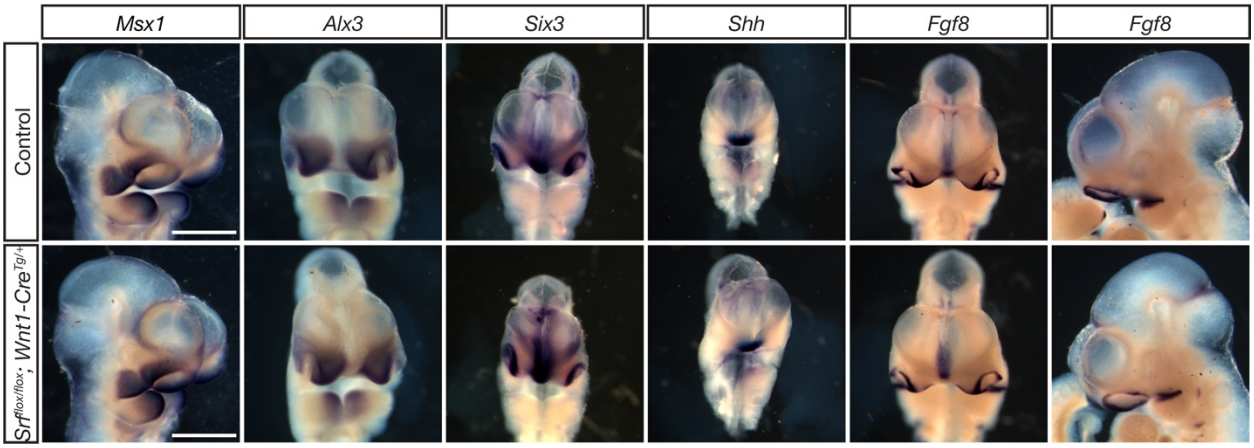

Figure 1 Supplement 1
Srf *NC conditional mutants do not show early patterning defects*
E10.5 embryos subject to *in situ* hybridization using probes against *Msx1, Alx3, Six3, Shh,* and *Fgf8* showed no significant differences between *Srf* NC conditional mutants and control littermates. *Msx1* embryos are shown in ¾ view to highlight maxillary expression. *Fgf8* embryos are shown in frontal and profile views to highlight the ventral forebrain and mandibular expression domains, respectively. Scale bar represents 500 µm.

We next sought to identify differentially expressed genes (DEGs) through bulk RNA-sequencing of control and mutant frontonasal prominences (FNP, i.e. MNP + LNP) and mandibles at E11.5. To confirm the quality of the dataset and suitability of the analysis pipeline, we first compared mandible versus FNP gene expression among all samples and identified differentially expressed transcripts encoding 4084 DEGs ($q \leq 0.05$, Wald test), among them known regulators of mandible or FNP identity, such as *Hand2* and *Six3* (Figure 1 Supplement 2A-B). Principal component analysis showed strong separation of the samples by tissue (Figure 1 Supplement 2C). We next identified DEGs in control versus *Srf*$^{flox/flox}$*; Wnt1-Cre*$^{Tg/+}$ mandibles and FNPs. Mandibles showed 40 DEGs and FNPs 219 ($q \leq 0.05$, Wald test). A joint model including both tissue samples and accounting for tissue-of-origin identified 381 DEGs (Figure 1D-E). *Srf* itself was among

166 the top DEGs, confirming efficient conditional deletion in the cranial NC (Figure 1D-E,

167 Figure 1 Supplement 2D).

168

Figure 1 Supplement 2

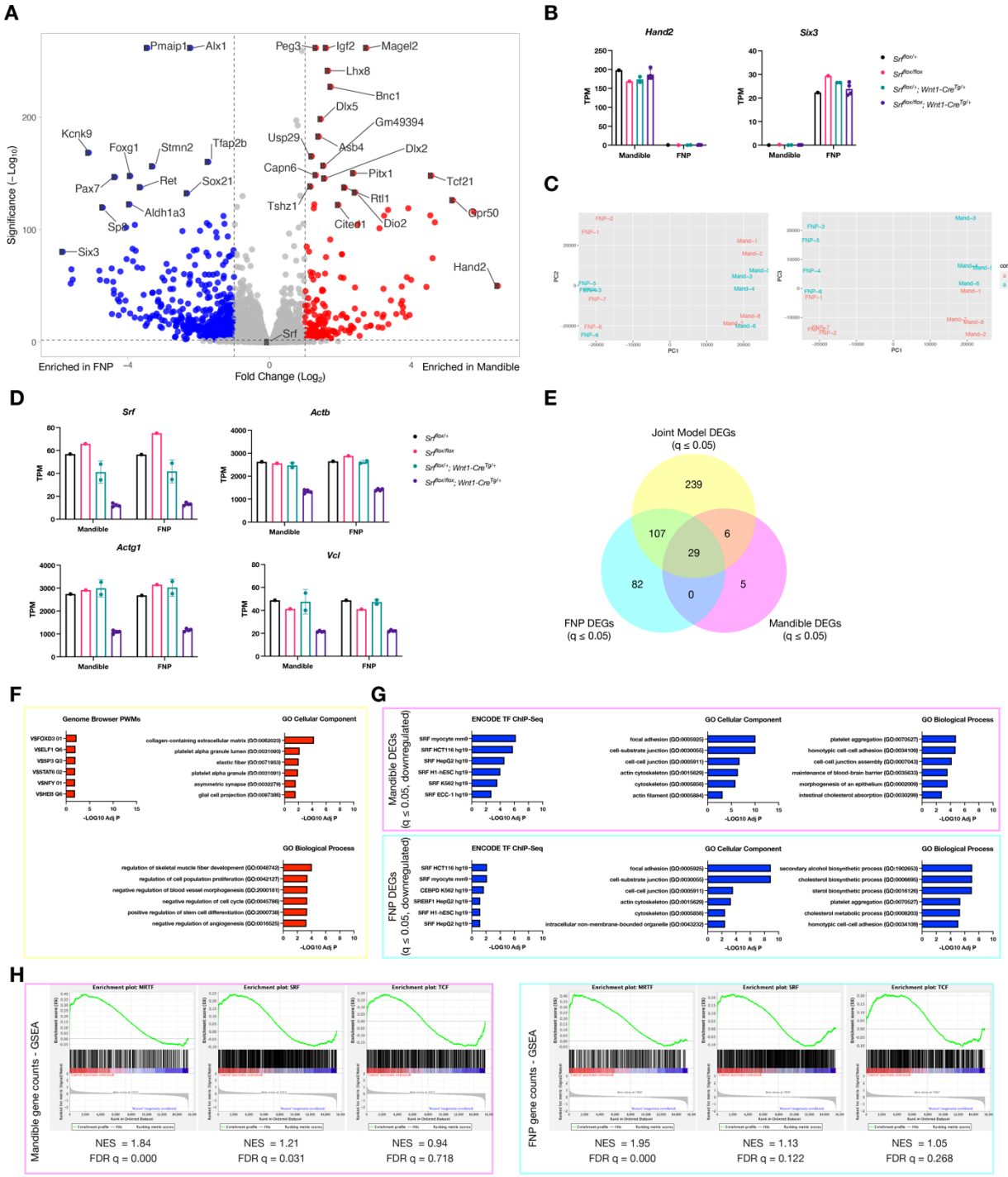

169

Figure 1 Supplement 2
Additional data related to craniofacial RNA-Seq
(A) Volcano plot showing genes enriched in mandible (red) versus FNP (blue) tissue. (B) Individual transcripts per million reads (TPM) values for *Hand2* and *Six3* plotted by genotype, showing the expected tissue enrichment. (C) PCA plots for the individual samples showing PCA1 vs PCA2 (left) and PCA1 vs PCA3 (right) indicate separation of the samples by tissue (PCA1) and genotype (PCA3). Samples are color-coded by genotype. (D) TPM values of *Srf* and several affected genes plotted by genotype. While *Srf* levels vary somewhat among the non-clefted control genotypes, downstream targets are only affected in the conditional mutants. (E) Overlap of DEGs from mandible (pink), FNP (cyan), and a joint model using both tissues (yellow). (F) Enrichr GSEA for upregulated genes with $q \leq 0.05$ and $Log2FC \geq 0.25$ from the joint model shows little enrichment and such genes may therefore be indirect targets of SRF. (G) Enrichr GSEA using a list of genes with $q \leq 0.05$ and $Log2FC \leq -0.25$ from each tissue showing similar terms to the joint model, with the exception of cholesterol-related GO terms specific to the FNP dataset. (H) GSEA for mandible and FNP samples compared to known SRF, MRTF, and TCF targets (Esnault et al., 2014; Gualdrini et al., 2016) showing preferential enrichment for MRTF targets in both datasets. Columns are the mean and error bars represent the standard deviation in (B) and (D).

The most differentially expressed genes primarily encoded cytoskeletal genes that were known targets of SRF-MRTF activity, including *Actg1*, *Cnn2*, *Vcl*, *Actb*, and *Cfl1* (Figure 1D-E). We subjected a more stringent list of 43 downregulated and 36 upregulated genes with $q \leq 0.05$ and $Log2FC \geq 0.25$ to gene set enrichment analysis using the online tool Enrichr (Xie et al., 2021). Downregulated genes were enriched for cytoskeletal GO terms and SRF-binding motifs (Figure 1F), whereas upregulated genes showed little enrichment for either TF motifs or GO terms and may not be direct SRF targets (Figure 1 Supplement 2F). We then used gene set enrichment analysis to compare our results with known targets of SRF, MRTF, and TCF (Esnault et al., 2014; Gualdrini et al., 2016) (Supplementary File 1). All three gene lists showed enrichment in our dataset, but the MRTF list was most significantly enriched (Figure 1G). Furthermore, limiting this comparison to DEGs with $q \leq 0.05$, genes bound by MRTF or MRTF and TCF were more significantly affected (higher fold change) than those bound by TCF alone (Figure 1H-I).

We also performed these analyses on the individual FNP and Mandible datasets that yielded similar enrichment for SRF motifs, cytoskeleton-related GO terms, and a stronger enrichment for known MRTF targets than for TCF targets (Figure 1 Supplement 2G-H). The one major difference between the tissues was that the FNP dataset contained a group of uniquely affected genes that enriched for terms related to cholesterol metabolism, but these were not further investigated (Figure 1 Supplement 2G, GO Biological Process).

In summary, our gene expression analysis found that the genes most affected by loss of *Srf* in both mandible and FNP were enriched for cytoskeleton-related established SRF-MRTF targets. These data, coupled with our previous observations that *Pdgfra* interacted genetically with *Srf* in NC and PDGF stimulation promoted SRF-MRTF complex formation, led us to hypothesize that SRF-MRTF interactions would be critical for midfacial development.

Srf$^{\alpha I/\alpha I}$ *succumb during early organogenesis with cardiovascular defects.* In order to test the requirement for SRF-MRTF interactions genetically, we introduced four knock-in point mutations to the αI helix of the SRF DNA-binding domain, previously shown to disrupt SRF-MRTF-DNA ternary complex formation while leaving SRF-TCF-DNA complex formation unaffected (Figure 2 Supplement 1A-C) (Hipp et al., 2019; Zaromytidou et al., 2006). Underscoring their importance, we found these residues are conserved in *Srf* orthologs from human to sponge, though they are intriguingly less well-conserved in clades lacking a readily identifiable *Mrtf* ortholog (Figure 2 Supplement 2). We included

207 an N-terminal 3xFLAG tag in the *Srf*$^{\alpha I}$ allele. As a control, we generated a separate *Srf*^{FLAG}

208 tagged line without the αI helix mutations.

209

Supplementary Figure 2 Supplement 1

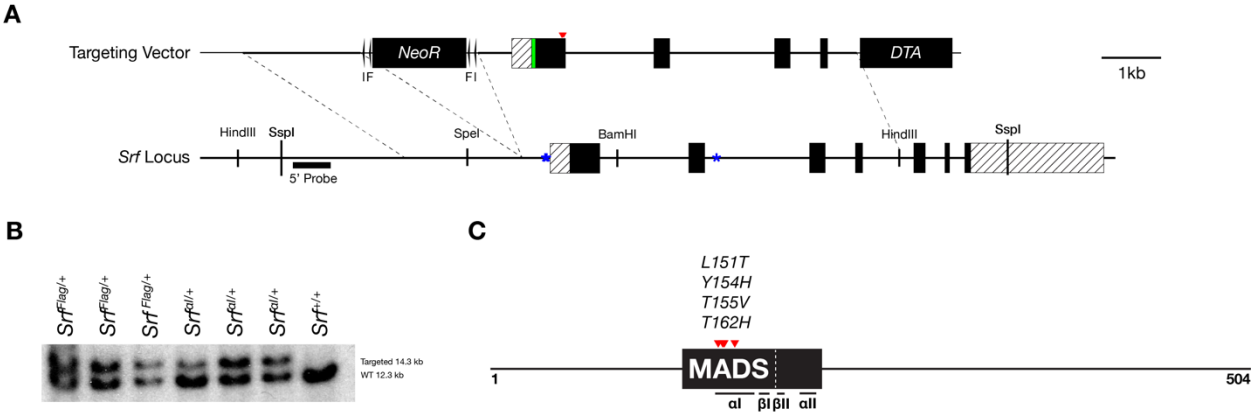

210

Figure 2 Supplement 1

Targeting strategy and validation for Srf^{Flag} *and* Srf$^{\alpha I}$ *alleles*

(A) A diagram of the targeting vector and the *Srf* locus. Homology arms containing an N-terminal 3x FLAG tag with or without mutated SRF αI residues were cloned into a targeting vector containing a *Pgk-NeoR* cassette flanked by loxP (I) and FRT (F) sequences. Dotted lines demarcate the homology arms relative to the endogenous locus. Exons are dark and UTR regions are striped. The FLAG tag is green and the location of the SRF αI residues is marked by red arrowheads. Autoregulatory CarG elements at -62 bp, -82 bp, and +2800 bp are marked by blue asterisks. (B) Southern blot of SspI digested targeted clones and WT genomic DNA blotted with the P32 labeled DNA probe indicated in (A). (C) Diagram of mouse SRF protein showing the DNA-binding domain as a dark box, the core MADS domain within it is labeled, subdomains are indicated underneath, and the SRF αI mutations are red arrowheads. Domains are based on Zaromytidou et al. (2006) with amino acid numbers adjusted for mouse. The 3x FLAG tag (not shown) was inserted just downstream of the start codon.

211

212

Figure 2 Extended Data 2

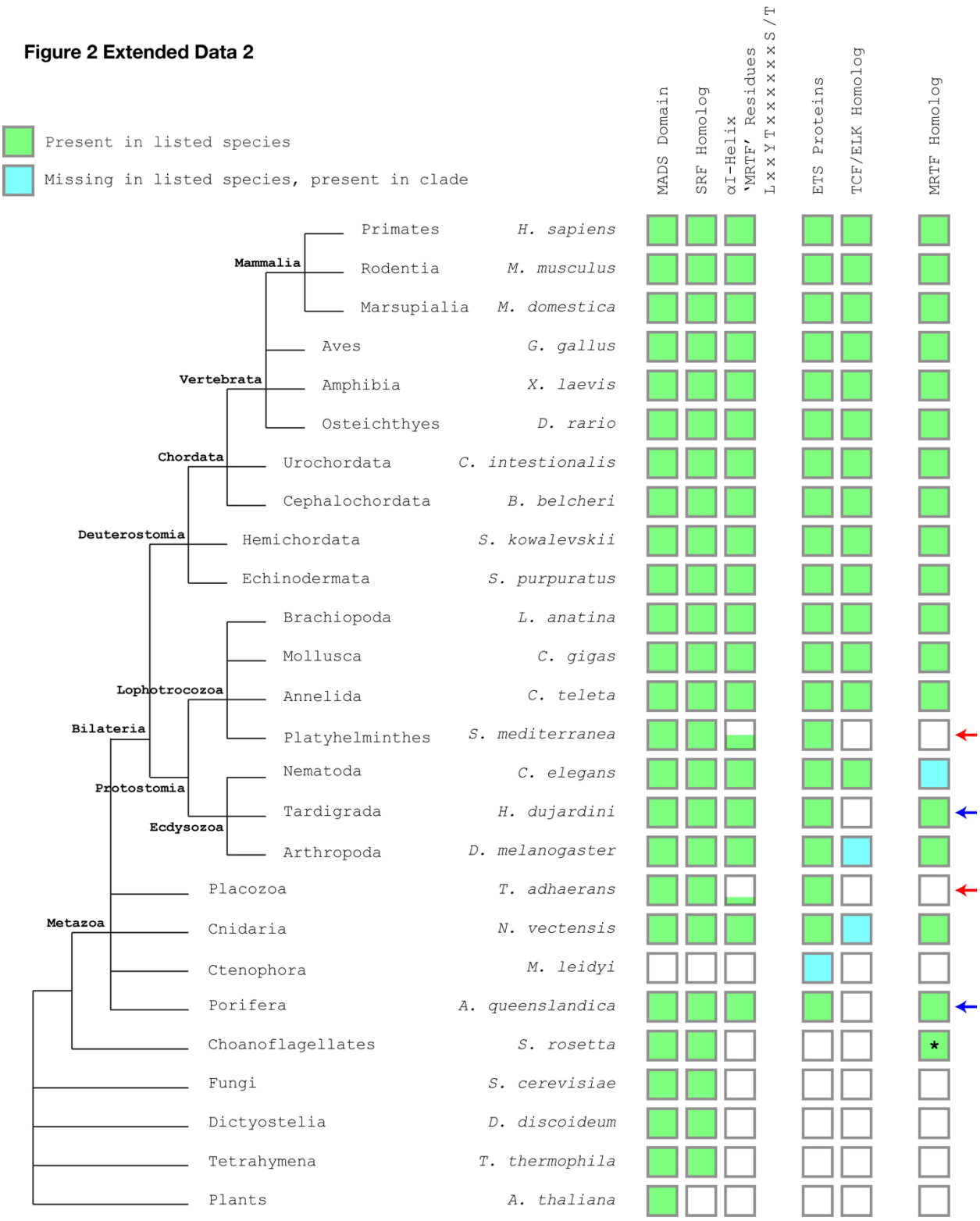

Figure 2 Supplement 2

SRF αI helix residues are highly conserved, but drift in clades lacking clear MRTF homologues

Representative species from major clades were subjected to BLASTP searches for mouse SRF, MRTF-B, and ELK1. The presence of a reciprocal best BLASTP hit is denoted in green. If a hit was negative, the search was repeated for the entire clade and identification of a hit is represented in cyan. Negative hits for ELK1 were researched with mouse ETS1 to find any ETS domain proteins. SRF αI residues were manually inspected and divergence is denoted by the height of the green bar in 25% increments, representing the four residues. Red arrows indicate clades where the SRF αI residues diverge that are also missing readily identifiable MRTF homologs, although some of these lineages also lack TCF/ELK homologs. Blue arrows indicate clades where SRF αI residues are conserved along with presence of an MRTF homolog, but that lack an obvious TCF/ELK homolog. The asterisk indicates that although a reciprocal best BLASTP hit for MRTF-B was found in *S. rosetta*, the hit was a short protein fragment and it is unclear if it represents a true MRTF homolog. The genus *Caenorhabditis* lacks an obvious MRTF homolog, but likely MRTF homologs can be found in other nematodes such as *B. malayi*, *L. loa*, and *O. flexuosa*.

214 *Srf*$^{FLAG/FLAG}$ mice were viable and fertile, confirming that neither the FLAG tag nor targeting
215 strategy affected development. In contrast, no *Srf*$^{\alpha I/\alpha I}$ mice were found at weaning age
216 (Table 1). Because we observed no stillborn or dying neonates, we examined embryos
217 at different stages. *Srf*$^{\alpha I/\alpha I}$ embryos were recovered in Mendelian ratios until E10.5 but
218 were easily identifiable from E9.5 onward due to their obvious morphological differences
219 from control littermates. Mutant embryos were slightly smaller at E9.5 and most had
220 turning defects that ranged in severity from incompletely turned to totally unturned (Figure
221 2A). This was accompanied by a wavy neural tube, as seen in many embryos with a
222 deficiency in mesoderm (Figure 2A, middle embryo) and some embryos showed a delay
223 in anterior neural tube closure, indicated by the open midbrain (Figure 2A). Mutant
224 embryos also had a missing or hypoplastic second pharyngeal arch (Figure 2A,
225 asterisks). Additionally, the yolk sac showed a crinkled appearance with numerous red
226 blood cells, but no obvious mature blood vessels, indicating the onset of primitive
227 hematopoiesis but not vasculogenesis (Figure 2B).

Genotype	Expected	Observed
Srf$^{+/+}$	7.75	12
Srf$^{al/+}$	15.5	19
Srf$^{al/al}$	7.75	0

χ^2 Test = 0.0044

Table 1

Srf$^{al/al}$ *embryos are not recovered at weaning*

Expected and recovered numbers of embryos of each genotype at weaning (P21). No homozygous mutant embryos were recovered.

228

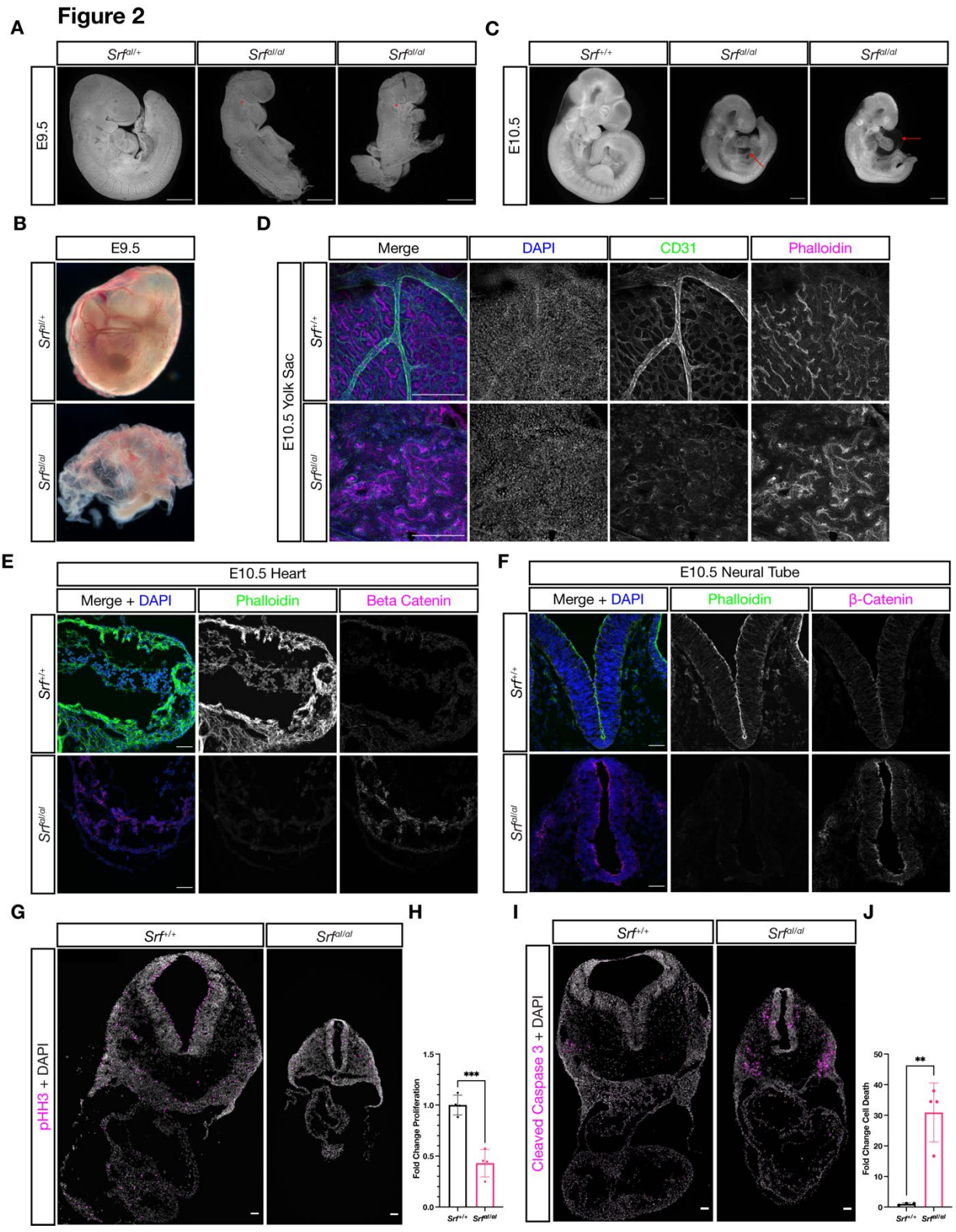

Figure 2

Srf$^{\alpha I/\alpha I}$ *embryos succumb at E10.5 with numerous defects*

(A) DAPI stained E9.5 embryos of the indicated genotypes show that compared to *Srf*$^{\alpha I/+}$ embryos, *Srf*$^{\alpha I/\alpha I}$ embryos are growth retarded, incompletely turned, have short and disorganized tails, a wavy neural tube, delayed anterior neural tube closure, and a hypoplastic or missing second pharyngeal arch (red asterisk). Scale bar represents 500 μm. (B) Brightfield images of E9.5 yolk sacs indicate defective vasculogenesis in mutant embryos. (C) DAPI stained E10.5 embryos show more extensive growth retardation, a distended heart tube, and pericardial edema (red arrow). Scale bar represents 500 μm. (D) Immunofluorescent staining of E10.5 yolk sacs shows that mutant yolk sacs lack a remodeled vascular plexus or any large vessels. Images are representative of n=4 embryos of each genotype. Scale bar represents 250 μm. (E) Transverse sections through E10.5 embryos at the level of the heart show reduced F-actin intensity via phalloidin staining and increased non-nuclear β-Catenin levels. Images are representative of n=4 embryos of each genotype. Scale bar represents 50 μm. (F) A similar pattern Is seen in the neural tube. Scale bar represents 50 μm. (G) Cell proliferation, indicated through phospho-Histone H3 (Ser10) (pHH3) staining, is reduced in mutant embryos. Scale bar represents 50 μm. (H) Quantitation of (G), n=4 each genotype. p=0.0005, Student's unpaired two-tailed t-test. (I) Cell death, revealed through cleaved caspase 3 staining, is dramatically increased in mutant embryos. Scale bar represents 50 μm. (J) Quantitation of (I), n=3 control embryos and n=4 mutant embryos. p=0.003, Student's unpaired two-tailed t-test. Columns are the mean and error bars represent the standard deviation in (H) and (J).

By E10.5, the anterior neural tube had closed but other defects remained or became apparent. Mutant embryos were much smaller than their wild-type or heterozygous littermates (Figure 2C). The developing heart tube appeared distended and thin, and most embryos showed pericardial edema (Figure 2C, arrows). The overall length of mutant embryos was shorter (Figure 2C) and a subset failed to turn, remaining inflected similar to the rightmost embryo in Figure 2A (data not shown). Whole-mount immunostaining of the yolk sac with the endothelial marker CD31/PECAM1 revealed that while wild type littermates had an extensively remodeled capillary plexus, including the presence of larger vessels, mutant yolk sacs had only a crude primitive capillary plexus, despite the presence of CD31-positive cells (Figure 2D). A reduction in F-Actin levels throughout mutant embryos, including the heart (Figure 2E) and neural tube (Figure 2F), was consistent with reduced SRF-MRTF-mediated transcription of cytoskeletal genes.

Interestingly, we noted a concomitant increase in non-nuclear β-Catenin levels (Figure 2E-F). Additionally, mutant embryos showed reduced cell proliferation and significantly increased cell death (Figure 2G-H).

While striking, the phenotype of *Srf*$^{\alpha I/\alpha I}$ embryos is less severe than that reported for *Srf* null mutants, which succumb from E6.5-E8.5 and do not induce expression of the mesoderm marker *T* (Arsenian et al., 1998). We generated homozygous *Srf*$^{-/-}$ embryos and found them to be delayed at E6.5 and E7.5 and were not recovered at later stages (data not shown), verifying the early lethality on our genetic background and thus confirming the difference in severity between the *Srf*$^{-}$ and *Srf*$^{\alpha I}$ alleles.

The Srf^{-} *and* Srf$^{\alpha I}$ *alleles cause similar defects in the anterior mesodermal lineage.* In order to make a second comparison between the *Srf*$^{\alpha I}$ and *Srf*$^{-}$ alleles, we generated *Srf*$^{flox/flox}$*; Mesp1*$^{Cre/+}$ and *Srf*$^{\alpha I/flox}$*; Mesp1*$^{Cre/+}$ embryos and assessed them at E9.5 and E10.5. *Mesp1-Cre* directs recombination in anterior mesoderm, including cardiac mesoderm. This is a tissue where SRF-MRTF interactions are known to be required, particularly through SRF-Myocardin activity in the developing heart and vascular smooth muscle (Li et al., 2003; Miano et al., 2004; Niu et al., 2005; Parlakian et al., 2004).

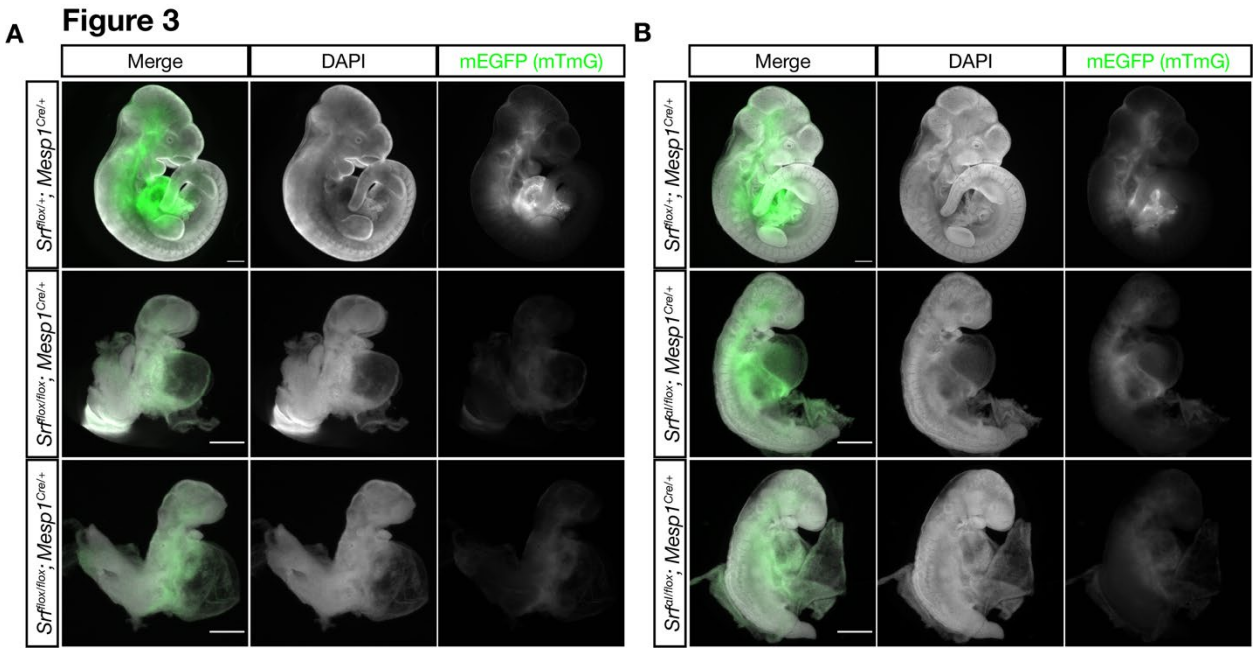

Figure 3
The Srf$^{\alpha l}$ *and Srf^{flox} alleles exhibits similar defects in anterior mesoderm*
(A) E10.5 littermate embryos were stained with DAPI and imaged. Loss of *Srf* in the *Mesp1-Cre* lineage causes embryos to be undersized with pericardial edema, hypoplastic hearts, and turning defects. Phenotype observed in n=3/3 mutant embryos. (B) A similar experiment in which *Srf$^{\alpha l}$* is the only *Srf* allele expressed in the *Mesp1-Cre* lineage. These embryos appear comparable to the mutant embryos in (A), though they are clearly less severely affected as they are slightly larger and partially turned. Phenotype observed in n=3/3 mutant embryos. Scale bar represents 500 μm in all images. Note the 2x higher crop in mutant embryos to better illustrate phenotypes.

Both *Srf$^{flox/flox}$; Mesp1$^{Cre/+}$* and *Srf$^{\alpha l/flox}$; Mesp1$^{Cre/+}$* embryos were inviable after E10.5 and exhibited similar phenotypes. Mutant embryos were small, had turning defects (or arrested prior to or during the turning process), pericardial edema, and hypoplastic hearts. They appeared quite similar to *Srf$^{\alpha l/\alpha l}$* embryos and phenocopied *Myocd* mutants (Figure 3A-B) (Li et al., 2003). Notably, although *Srf$^{\alpha l/flox}$; Mesp1$^{Cre/+}$* and *Srf$^{flox/flox}$; Mesp1$^{Cre/+}$* embryos were broadly similar, *Srf$^{flox/flox}$; Mesp1$^{Cre/+}$* embryos were more strongly affected, being reproducibly smaller and completely unturned. Although these embryos were generated from separate crosses, precluding direct comparisons, the observations were

consistent across multiple litters. We conclude from this analysis that the *Srf*$^{\alpha l}$ allele is less severe than the *Srf*$^{-}$ allele, but nevertheless represents a significant curtailment of SRF activity. Moreover, because *Srf*$^{\alpha l/flox}$*; Mesp1*$^{Cre/+}$ and *Srf*$^{\alpha l/\alpha l}$ embryos are so similar, the *Srf*$^{\alpha l/\alpha l}$ phenotype is not a secondary consequence of placental insufficiency, a common cause of cardiovascular and neural phenotypes (Perez-Garcia et al., 2018), as *Mesp1*$^{Cre/+}$ labels anterior embryonic and extraembryonic (i.e. yolk sac) mesoderm, but not the trophectoderm-derived placenta (Saga et al., 1999).

Srf$^{\alpha l/flox}$; Wnt1-Cre$^{Tg/+}$ *embryos do not display craniofacial defects at E13.5.* We next asked whether *Srf*$^{\alpha l/flox}$*; Wnt1-Cre*$^{Tg/+}$ embryos would display similar defects to *Srf*$^{flox/flox}$*; Wnt1-Cre*$^{Tg/+}$ embryos, as we expected. Surprisingly, these embryos appeared completely normal at E13.5 (Figure 4A), when *Srf*$^{flox/flox}$*; Wnt1-Cre*$^{Tg/+}$ embryos are already dying and display obvious craniofacial abnormalities.

We tested whether the *Srf*$^{\alpha l}$ allele was behaving as expected in the NC lineage using MEPM cells cultured from E13.5 *Srf*$^{\alpha l/flox}$*; Wnt1-Cre*$^{Tg/+}$*; ROSA26*$^{TdT/+}$ (mutant) and *Srf*$^{flox/+}$*; Wnt1-Cre*$^{Tg/+}$*; ROSA26*$^{TdT/+}$ (control) palatal shelves (Figure 4B). We assessed the expression of genes preferentially regulated by SRF-TCF activity, such as the IEGs, and those regulated by SRF-MRTF activity, namely cytoskeletal genes. At the protein level, immunofluorescent staining of MEPM cells for F-actin and smooth muscle actin (SMA) showed reduced intensity in mutant cell lines compared to control lines (Figure 4C). We also assessed gene expression at the mRNA level by qPCR in starved and serum-stimulated lines. While we noted no significant changes in the expression of the IEGs

294 *Egr1* and *Fos* (Figure 4D), levels of *Tagln* (SM22) and *Acta2* (the gene encoding SMA)
295 were significantly downregulated in both conditions, and we noted a downward trend in
296 *Vcl* expression (Figure 4D). *Srf* itself was also significantly downregulated, likely due to
297 autoregulation via the several CArG elements at the *Srf* locus (Figure 4D, Figure 2
298 Supplement 1A). We confirmed that MRTF-A translocated to the nucleus in response to
299 serum in control and mutant cell lines (Figure 4 Supplement 1A-B).

Figure 4

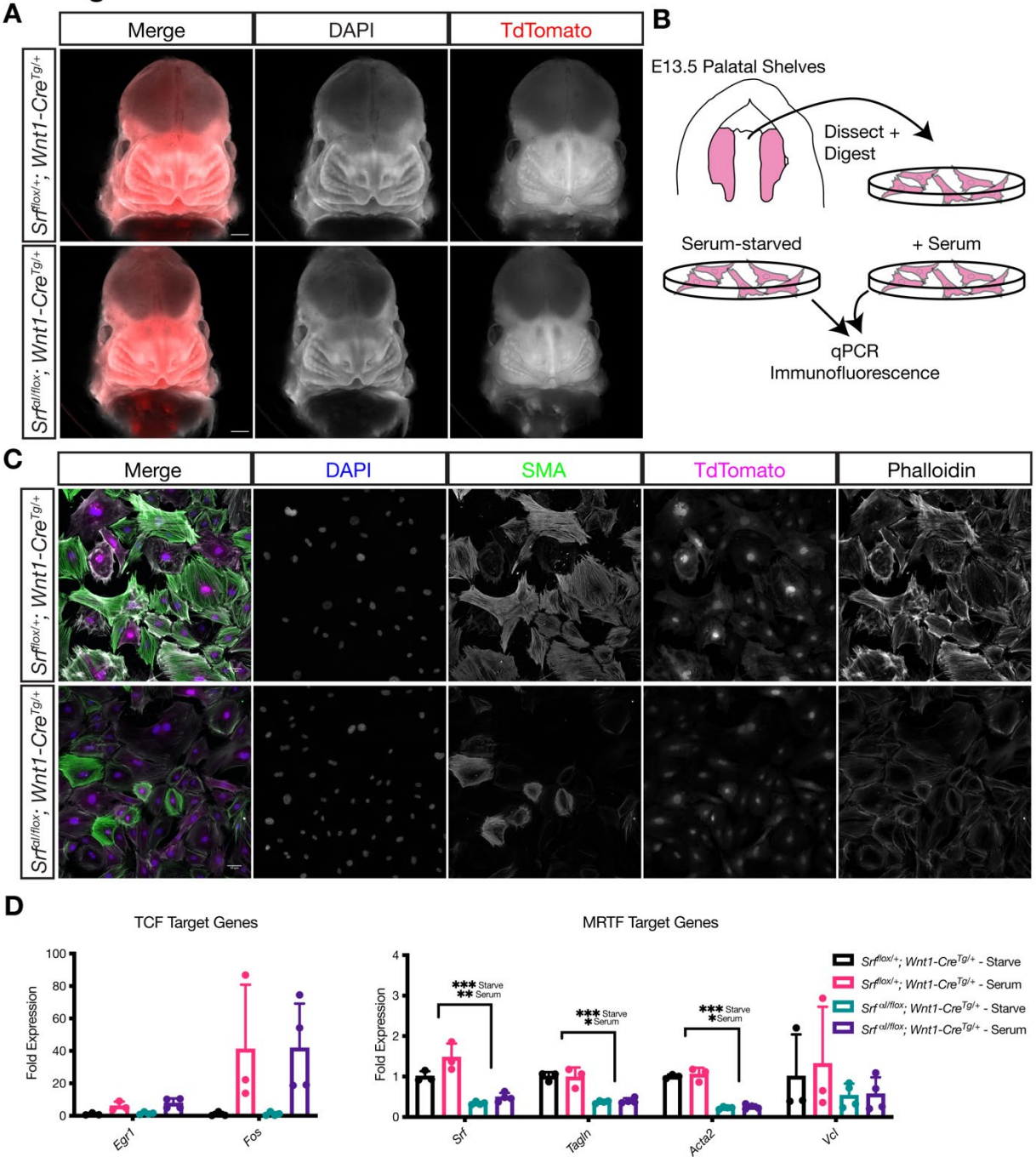

300

Figure 4
NC Srf$^{\alpha l}$ *conditional mutants are normal at E13.5*
(A) DAPI stained E13.5 littermate embryos carrying a *ROSA26*$^{TdT/+}$ Cre reporter show no apparent craniofacial defects in conditional mutants. Scale bar represents 500 μm. (B) Diagram illustrating the culture of MEPM cells. (C) Immunofluorescent staining of passage 2 MEPM cells shows reduced F-actin and SMA fluorescence in mutant cells compared to cells from heterozygous littermate control embryos. Scale bar represents 50 μm. (D) qPCR from serum-starved and serum-stimulated MEPM cells indicates no difference in IEG expression (*Egr1, Fos*) but a significant defect in *Srf* (q=0.00042 starve, q=0.0095 serum), *Tagln* (q=0.00038 starve, q=0.013 serum), and *Acta2* (q=0.000011 starve, q=0.0027 serum) expression and a downward trend in *Vcl* expression. Values are fold expression of control starved cells. N=3 control lines and n=4 mutant lines. Significance was determined by Student's unpaired t-test with two-stage step-up correction (Benjamini, Krieger, and Yekutieli) for multiple comparisons. Columns are the mean and error bars represent the standard deviation.

Because *Srf* interacts genetically with *Pdgfra* in the NC and because SRF-MRTF transcriptional targets were suggested to be of particular importance downstream of PDGFRA signaling, we reasoned that the *Srf*$^{\alpha l}$ allele might also interact genetically with *Pdgfra* in this tissue (Vasudevan & Soriano, 2014). To test this possibility, we generated *Srf*$^{\alpha l/+}$*; Pdgfra*$^{H2B\text{-}EGFP/+}$*; Wnt1-Cre*$^{Tg/+}$ triple heterozygous male mice and crossed them with *Srf*$^{flox/flox}$*; ROSA26*$^{TdT/TdT}$ mice but did not observe facial clefting in embryos of any genotype (data not shown).

In summary, cells from *Srf*$^{\alpha l/flox}$*; Wnt1-Cre*$^{Tg/+}$ embryos show the expected changes in gene expression, yet the embryos themselves show no outward signs of the severe craniofacial phenotypes observed in *Srf*$^{flox/flox}$*; Wnt1-Cre*$^{Tg/+}$ embryos at this stage.

Figure 4 Supplement 1

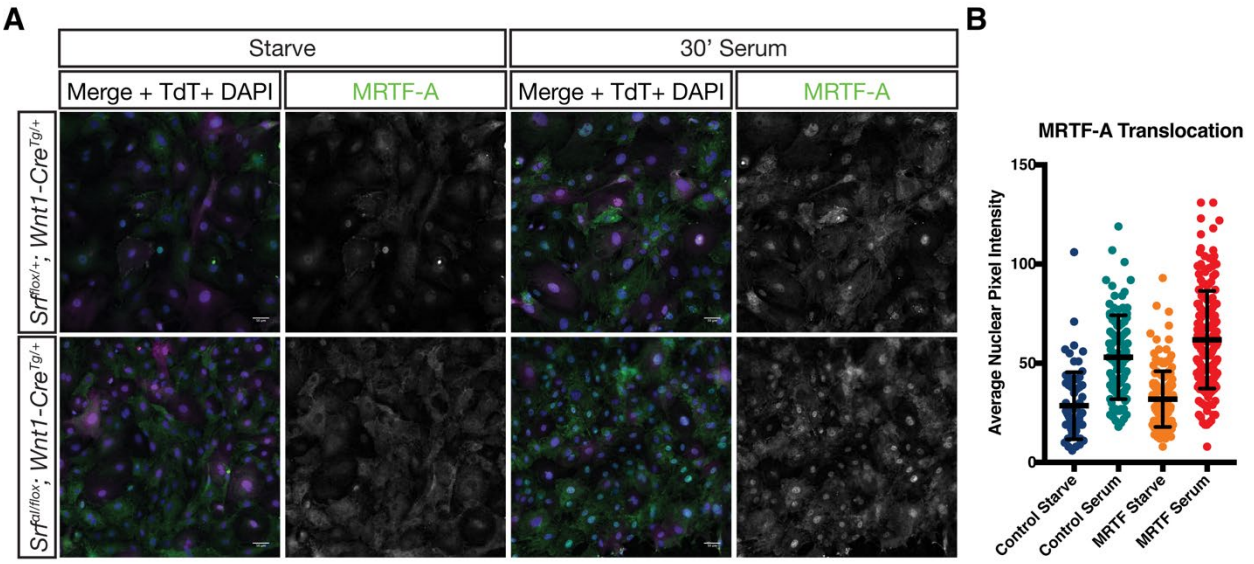

Figure 4 Supplement 1
MRTF-A translocates to the nucleus normally in response to serum stimulation in mutant MEPM cells
(A) Serum starved or stimulated P2 primary MEPM cells from *Srf$^{\alpha I/flox}$; Wnt1-Cre$^{Tg/+}$; ROSA26$^{TdT/+}$* (mutant) and *Srf$^{flox/+}$; Wnt1-Cre$^{Tg/+}$; ROSA26$^{TdT/+}$* (control) embryos were stained for MRTF-A and DAPI. (B) Nuclear MRTF-A levels were quantified using the DAPI channel to identify nuclei. Dots represent individual cells pooled from n=2 unique cell lines for each genotype. Horizontal bars are the mean and error bars represent the standard deviation.

Srf$^{\alpha I/flox}$; Wnt1-Cre$^{Tg/+}$ *mice succumb in the early postnatal period with outflow tract defects. Srf$^{\alpha I/flox}$; Wnt1-Cre$^{Tg/+}$* embryos survived until birth, after which they died within the first two days of life with visible cyanosis (Figure 5A). We examined E18.5 skeletal preparations for defects in patterning or ossification that may arise after E13.5. Mutant skulls were smaller than in control littermates, but the craniofacial skeleton was patterned normally indicating a developmental delay at this timepoint (Figure 5 Supplement 1). To determine the underlying cause of cyanosis, we examined the cardiac outflow tract at P0 as the smooth muscle in this region is NC-derived and responsible for proper remodeling

of the aortic arch vessels during development. We found a highly penetrant (9/14) patent ductus arteriosus (PDA) exclusively in *Srf*$^{\alpha l/flox}$*; Wnt1-Cre*$^{Tg/+}$ neonates (Figure 5B-C). In this condition, the embryonic shunt from the pulmonary artery to the aorta, the ductus arteriosus, fails to close after birth, making circulation to the lungs inefficient and likely explaining the postnatal cyanosis. We also noted one instance of aberrant right subclavian artery, in which the right subclavian artery originates from the descending aorta instead of the brachiocephalic artery, which only supplies the right common carotid artery in this condition. We also inspected P0 mice from a similar cross on a *Pdgfra*$^{H2B\text{-}EGFP/+}$ background to assess whether heterozygosity for *Pdgfra* would exacerbate phenotypes at this stage, but neonates were recovered in the expected Mendelian ratios with similar outflow tract defects (Figure 5 Supplement 2A-B). Two *Srf*$^{\alpha l/flox}$*; Wnt1-Cre*$^{Tg/+}$*; Pdgfra*$^{+/+}$ from this set of crosses displayed a more severe outflow tract defect: right aortic arch with mirror image branching (2/9; Figure 5C, far right).

Figure 5

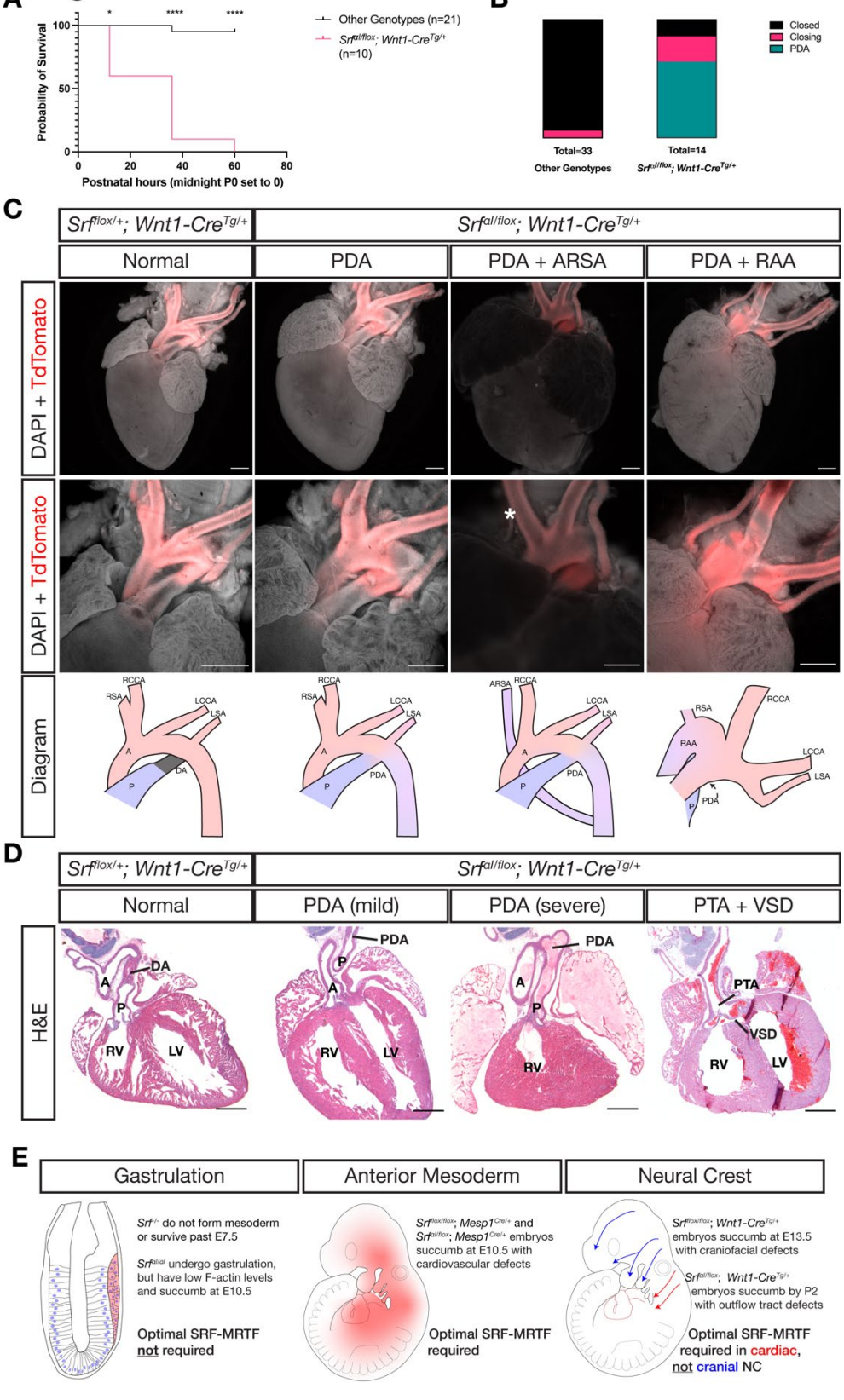

335

Figure 5

NC Srf$^{\alpha I}$ *conditional mutants succumb postnatally with outflow tract defects*

(A) Kaplan-Meyer survival curve for neonatal *Srf$^{\alpha I/flox}$; Wnt1-Cre$^{Tg/+}$* (Mutant) compared to littermates of all other genotypes (Control). Significance was computed at each timepoint using a Mantel-Cox log-rank test. P0 p=0.0142, P1 p<0.0001, P2 p<0.0001. (B) Stacked columns showing the distribution of PDA-related phenotypes in *Srf$^{\alpha I/flox}$; Wnt1-Cre$^{Tg/+}$* neonates compared to littermates of all other genotypes. (C) DAPI-stained postnatal day 0 (P0) hearts carrying a *ROSA26$^{Tdt/+}$* Cre lineage reporter showing the entire heart (top row) and the outflow tract region (bottom row). Examples of mutant phenotypes such as PDA, ARSA, and RAA. An asterisk indicates where the missing right subclavian artery should be. Note the ARSA mouse had succumbed prior to dissection and the image is dimmer due to the presence of clotted blood. The outflow tract defects are schematized below. Scale bar represents 500 μm. (D) Hematoxylin and eosin-stained frontal sections through P0 hearts showing mild to severe PDA and an example of VSD and PTA in mutants. Scale bar represents 500 μm. (E) Summary of our results, showing the requirements for SRF versus SRF$^{\alpha I}$ in different tissues and timepoints. A, aorta; ARSA, aberrant right subclavian artery; DA, ductus arteriosus; LCA, left common carotid artery; LSA, left subclavian artery; LV, left ventricle; P, pulmonary artery; PDA, patent ductus arteriosus; PTA, persistent truncus arteriosus; RAA, right aortic arch with mirror image branching; RCA, right common carotid artery; RSA, right subclavian artery.

Sections through *Srf$^{\alpha I/flox}$; Wnt1-Cre$^{Tg/+}$* and control *Srf$^{flox/+}$; Wnt1-Cre$^{Tg/+}$* hearts confirmed the macroscopically observed PDAs and also revealed one instance of ventricular septal defect (VSD) with persistent truncus arteriosus (PTA), a failure of the truncus arteriosus to fully septate into the aorta and pulmonary artery, out of ten mutant hearts examined (Figure 5D). Mutant embryos that survived the first several hours of life had a milk spot, indicating they did not have pronounced defects in olfaction or the craniofacial bones, nerves, and muscles required for suckling. Thus, while the *Srf$^{\alpha I}$* allele is surprisingly well-tolerated in the cranial NC lineage throughout most of development, it is required in the cardiac NC-derived smooth muscle of the cardiac outflow tract to support postnatal life, highlighting a critical role for SRF-MRTF interactions in this particular NC lineage (Figure 5E).

Figure 5 Supplement 1

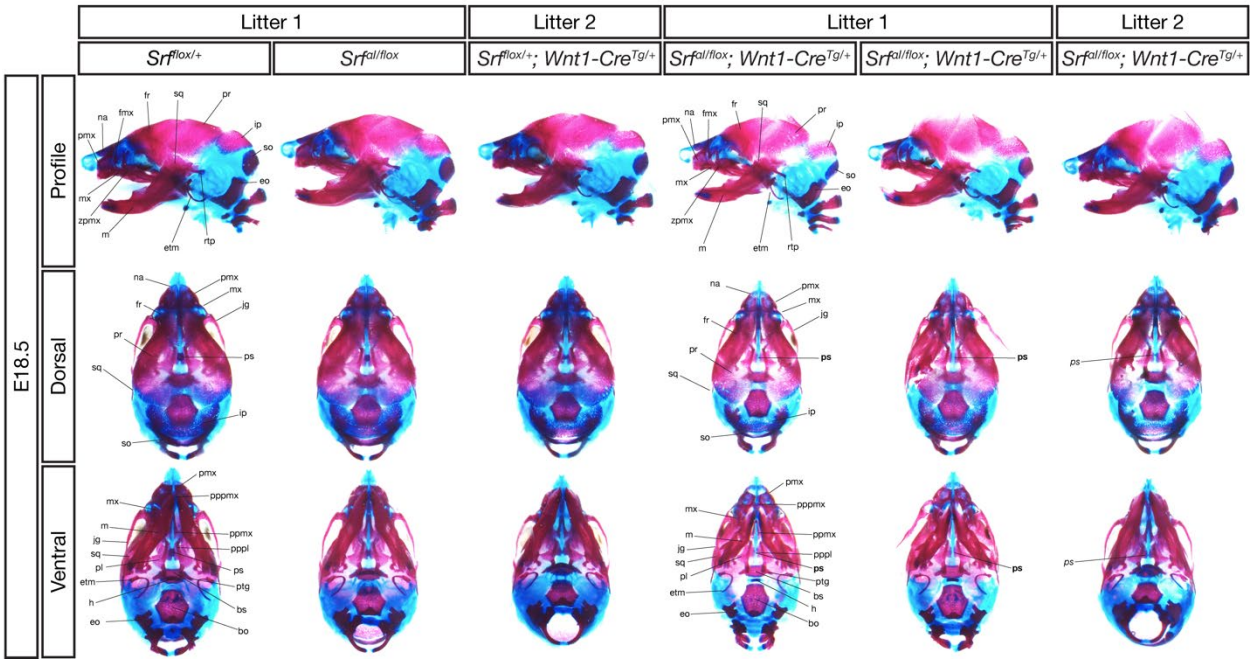

348

Figure 5 Supplement 1

E18.5 conditional mutant skulls are delayed but correctly patterned

Alizarin red (bone) and alcian blue (cartilage) stained E18.5 skulls of the indicated genotypes from two litters are shown. All three conditional mutant embryos were smaller than their control littermates and had less extensive ossification. However, all the indicated bones were present in each genotype, except for the presphenoid bone, which was missing in 2/3 mutants (location of missing bone indicated in bold) and rudimentary in one (italics). Bo, basioccipital; bs, basisphenoid; eo, exoccipital; etm, ectotympanic; fmx, frontal process of maxilla; fr, frontal; h, hyoid; ip, interparietal; jg, jugal; m, mandible; mx, maxilla; na, nasal; pl, palatine; pmx, premaxilla; ppmx, palatal process of maxilla; pppl, palatal process of palatine; pppmx, palatal process of premaxilla; pr, parietal; ps, presphenoid; ptg, pterygoid; rtp, retrotympanic process; so, supraoccipital; sq, squamosal; zpmx, zygomatic process of maxilla.

349

350

Figure 5 Supplement 2

A

Genotype	Expected	Observed
Srf$^{flox/+}$; *Pdgfra*$^{+/+}$; *Wnt1-Cre*$^{+/+}$	7.25	7
Srf$^{flox/+}$ *Pdgfra*$^{H2B\text{-}EGFP/+}$; *Wnt1-Cre*$^{+/+}$	7.25	10
Srf$^{\alpha I/flox}$; *Pdgfra*$^{+/+}$; *Wnt1-Cre*$^{+/+}$	7.25	7
Srf$^{flox/+}$; *Pdgfra*$^{+/+}$; *Wnt1-Cre*$^{Tg/+}$	7.25	5
Srf$^{flox/+}$; *Pdgfra*$^{H2B\text{-}EGFP/+}$; *Wnt1-Cre*$^{Tg/+}$	7.25	9
Srf$^{\alpha I/flox}$; *Pdgfra*$^{H2B\text{-}EGFP/+}$; *Wnt1-Cre*$^{+/+}$	7.25	9
Srf$^{\alpha I/flox}$; *Pdgfra*$^{+/+}$; *Wnt1-Cre*$^{Tg/+}$	7.25	5
Srf$^{\alpha I/flox}$; *Pdgfra*$^{H2B\text{-}EGFP/+}$; *Wnt1-Cre*$^{Tg/+}$	7.25	6

χ^2 Test = 0.833

B

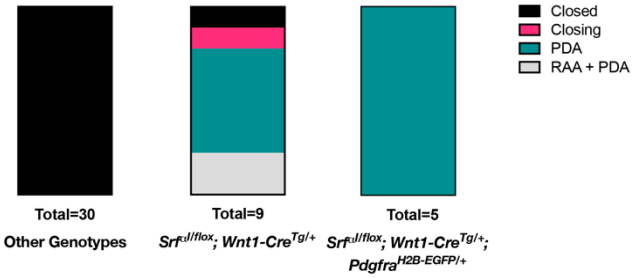

Figure 5 Supplement 2
Pdgfra *and* Srf$^{\alpha I}$ *do not interact genetically in NC*
(A) Expected and recovered numbers of embryos of each genotype at birth (P0). No significant deviation from Mendelian ratios was observed. (B) PDA-related phenotypes in *Srf*$^{\alpha I/flox}$*; Wnt1-Cre*$^{Tg/+}$ neonates are not exacerbated by the loss of one copy of *Pdgfra*.

Discussion

SRF is a ubiquitously expressed transcription factor whose transcriptional output is strongly influenced by its cofactors, the TCFs and MRTFs. These cofactors, in turn, are regulated both by specific expression patterns (e.g. *Myocd* specifically in muscle) and by signaling pathways, such as ERK1/2 and PI3K (Posern & Treisman, 2006) (Figure 1A). We sought to better understand the relationship between SRF, its cofactors, and mutant phenotypes in both a general and a tissue-specific manner.

Our previous study demonstrated a requirement for *Srf* in the NC lineage (Vasudevan & Soriano, 2014), so we first investigated how loss of SRF in this tissue affected gene expression. We found normal early NC patterning but misexpression of cytoskeleton-related genes in *Srf*$^{flox/flox}$*; Wnt1-Cre*$^{Tg/+}$ embryos (Figure 1C-F, Figure 1 Supplement 1, 2E). Comparing the DEGs with known SRF and cofactor targets showed particular

366 enrichment for MRTF targets in our datasets (Figure 1G-H, Figure 1 Supplement 2F-G),
367 consistent with SRF's well-known function regulating cytoskeletal genes and the
368 dominant role of MRTF cofactors in the serum response (Esnault et al., 2014). To test the
369 supposition that SRF-MRTF activity would be the main driver of NC SRF activity, we made
370 a new *Srf*$^{\alpha l}$ mouse model harboring point mutations that specifically disrupt SRF-MRTF-
371 DNA complex formation (Zaromytidou et al., 2006).
372
373 Homozygous *Srf*$^{\alpha l/\alpha l}$ embryos died at E10.5 with defects in the yolk sac vasculature, heart,
374 and neural tube and exhibited reduced F-actin levels (Figure 2A-F). Both the timing of
375 lethality and gross appearance of the embryos strongly resemble *Myocd*$^{-/-}$ mutant mice
376 (Li et al., 2003). The phenotype is much less severe than *Srf*$^{-/-}$ embryos, however, which
377 die around E7.5 and fail to induce mesoderm (Arsenian et al., 1998; Niu et al., 2005).
378 Expression of the *Srf*$^{\alpha l}$ allele specifically in the *Mesp1*^{Cre} mesodermal lineage also
379 resulted in lethality at E10.5 and defects almost as severe as complete loss of *Srf* in this
380 same lineage (Figure 3). The similarity of the two alleles in the *Mesp1*^{Cre} lineage
381 compared against their strikingly different phenotypes in gastrula-stage embryos
382 suggested there may be time or tissue specific requirements for SRF-MRTF activity.
383
384 We went on to test the *Srf*$^{\alpha l}$ allele in the NC lineage, where we presumed it would be
385 critically important. Similar to the early embryo, expression of the *Srf*$^{\alpha l}$ allele was well
386 tolerated in NC and we found no facial cleft or bleb in our *Srf*$^{\alpha l/flox}$*; Wnt1-Cre*$^{Tg/+}$ mice, as
387 in *Srf*$^{flox/flox}$*; Wnt1-Cre*$^{Tg/+}$ mice (Figure 4A). The allele also failed to interact genetically
388 with *Pdgfra* in this lineage, suggesting PDGF signaling may rely on MRTF-independent

389 SRF activity (Figure 5 Supplement 2A-B). Nevertheless, this mutation in NC does have a
390 profound developmental effect as *Srf*$^{\alpha l/flox}$*; Wnt1-Cre*$^{Tg/+}$ mice completed gestation but
391 died by postnatal day 2 with visible cyanosis (Figure 5A). Examination of the cardiac
392 outflow tract revealed numerous defects including PDA, right aortic arch, and one
393 instance of VSD with PTA (Figure 5C-D). This result is reminiscent of mice with a
394 hypomorphic gene trap mutation in *Mrtfb* and mice carrying a conditional deletion of
395 *Myocd* in the NC (Huang et al., 2008; J. Li et al., 2005), both of which result in early
396 postnatal lethality due to defects in outflow tract development. Similarly, NC conditional
397 *Srf* mutants on a genetic background that permitted later development exhibit outflow
398 tract defects at E16.5 (Newbern et al., 2008). These studies and our own results together
399 highlight a critical role for SRF-MRTF interactions in cardiac NC development. A summary
400 of the tissue-specific sensitivities we found to loss of *Srf* or *Srf*$^{\alpha l}$ expression is depicted in
401 Figure 5E.
402
403 We considered three possible explanations for the tolerance of the *Srf*$^{\alpha l}$ allele in NC and
404 early embryo, which are not mutually exclusive. The first is that TCF factors play a more
405 important role than previously thought or can somehow compensate for loss of SRF-
406 MRTF activity. It is true that some SRF targets can be bound and regulated by both MRTF
407 and TCF factors (Esnault et al., 2014). However, most studies to date indicate that MRTFs
408 and TCFs not only compete for a common binding site on SRF, but mediate distinct and
409 opposing phenotypic outcomes, contractility and proliferation, respectively (Gualdrini et
410 al., 2016; Wang et al., 2004). Furthermore, TCF triple mutant embryos survive until E14.5
411 without obvious morphological defects (Costello et al., 2010). While we cannot rule out

412 the possibility that TCFs are the primary SRF cofactors in neural crest or function
413 redundantly to MRTFs without further genetic experiments, this explanation is difficult to
414 reconcile with the existing literature.
415
416 A second explanation is that non-muscle lineages may be able to function with minimal,
417 but not zero, SRF-MRTF activity. It is possible that the *Srf*$^{\alpha l}$ allele substantially impairs
418 but not does eliminate SRF-MRTF-DNA complex formation and functions as a hypomorph
419 in this respect. Biochemical assays for SRF-MRTF-DNA complex formation and single
420 molecule imaging of SRF using this allele indicate a substantial disruption of SRF-MRTF
421 activity, but 5-10% residual complex formation remained in the original description of the
422 αI helix mutations (Hipp et al., 2019; Zaromytidou et al., 2006). On one hand, our own
423 data demonstrate that homozygous *Srf*$^{\alpha l/\alpha l}$ embryos grossly phenocopy *Myocd*$^{-/-}$ mutants
424 (Figure 2) and *Srf*$^{\alpha l/flox}$*; Mesp1-Cre*$^{Tg/+}$ and *Srf*$^{flox/flox}$*; Mesp1-Cre*$^{Tg/+}$ embryos were similar,
425 though not identical (Li et al., 2003). On the other hand, double conditional mutants for
426 *Mrtfa/Mrtfb* largely *do* phenocopy *Srf* conditional mutants in several tissues (Cenik et al.,
427 2016; Guo et al., 2018; S. Li et al., 2005; Trembley et al., 2015). Therefore, we may be
428 observing differing dosage requirements for SRF-MRTF activity in distinct tissues. Muscle
429 lineages, such as cardiovascular cells affected by *Mesp1*^{Cre} and outflow tract smooth
430 muscle affected by *Wnt1-Cre,* may need optimal SRF-MRTF output and are therefore
431 strongly affected by the *Srf*$^{\alpha l}$ allele. Non-muscle lineages such as the cranial NC may
432 survive and develop properly with only residual SRF-MRTF transcription. Two predictions
433 of this model are that conditional ablation of *Mrtfa/Mrtfb* in NC would phenocopy loss of
434 *Srf* and conversely that non-muscle lineages where conditional ablation of *Mrtfa/Mrtfb*

yields *Srf*-like phenotypes, such as podocytes and epicardium, would be indifferent to the *Srf*$^{\alpha I}$ mutations.

The issue of SRF tissue-specific dosage effects may have relevance to human disease. A recent study performed targeting sequencing of *SRF* in nonsyndromic conotruncal heart defect patients and identified two novel mutations with reduced transcriptional output, one from a patient with VSD and the other with Tetralogy of Fallot with right aortic arch (Mengmeng et al., 2020). Thus, tuning of SRF output may modulate disease in a tissue-specific manner. Along these lines, mutations in *MYOCD* cause congenital megabladder and associated cardiovascular phenotypes such as PTA and VSD in humans, but monoallelic mutations affect only males whereas biallelic mutations affect both sexes (Houweling et al., 2019). Furthermore, heterozygosity for *FLNA*, a gene we found strongly affected by loss of *Srf* in mouse NC, causes the human disease Periventricular Heterotopia I and affected females present with PDA, whereas hemizygous males die during gestation (Fox et al., 1998). Intriguingly, NC-specific conditional knockout of *Flna* causes perinatal lethality with outflow tract defects in mice (Feng et al., 2006). It would be interesting to further explore the notion of tissue-specific thresholds for SRF-cofactor complexes in future studies.

A third explanation is that SRF functions with additional factors that regulate gene expression independent of or redundantly with MRTFs (and/or TCFs). Although MRTFs and TCFs are the most well-studied SRF cofactors, many other TFs have been shown to interact with SRF, including but not limited to Homeodomain proteins (Chen et al., 1996;

458 Chen et al., 2002; Grueneberg et al., 1992; Shin et al., 2002), GATA factors (Belaguli et
459 al., 2000; Morin et al., 2001), and Forkhead-family transcription factors (Freddie et al.,
460 2007; Liu et al., 2005), as well as the Initiator-binding protein TFII-I (Grueneberg et al.,
461 1997; Kim et al., 1998). Many of these studies were performed in muscle cells and it is
462 unclear which cofactors might act independently of MRTFs. However, several of these
463 genes or their orthologues are expressed in the cranial NC at E10.5 and E11.5, when
464 cleft formation begins in *Srf*$^{flox/flox}$*; Wnt1-Cre*$^{Tg/+}$ embryos (Minoux et al., 2017). One
465 candidate is the homeodomain protein PRRX1/PHOX1/MHOX, which was shown to form
466 complexes with SRF mediated by TFII-I (Grueneberg et al., 1997). Double mutants for
467 *Prrx1* and its orthologue *Prrx2* have defects of the craniofacial skeleton, aortic arch
468 arteries, and ductus arteriosus (Bergwerff et al., 2000; Lu et al., 1999). *Gtf2i* mutants (the
469 gene encoding TFII-I) rarely survive past E10.5 but can exhibit a facial cleft,
470 hemorrhaging, and hypoplastic pharyngeal arches (Enkhmandakh et al., 2009). Whether
471 SRF mediates transcription independent of MRTFs and TCFs, perhaps using additional
472 tissue-specific cofactors, would be exciting to determine.
473
474 In conclusion, we found that the primary transcriptional consequence of losing *Srf* in NC
475 was a defect in actin cytoskeleton-related gene expression. Using a novel *Srf*$^{\alpha I}$ allele to
476 perturb SRF's interactions with MRTFs, the primary cofactors regulating the cytoskeletal
477 transcription program, we uncovered a crucial role for SRF-MRTF activity in the cardiac
478 NC, but surprisingly found the mutation well-tolerated in the cranial NC. Further study will
479 be necessary to determine the relevant SRF-cofactor ensembles in different
480 developmental contexts.

Author Contributions

C.J.D. and P.S. designed the study. P.S. performed blastocyst injections and embryo transfers. P.S. and C.J.D. performed gene targeting and Southern blotting. C.J.D. carried out all the remaining experiments, data analysis, and figure preparation. C.J.D. and P.S. wrote the manuscript.

Acknowledgements

We thank the members of the Soriano lab, Robert Krauss, Sergei Sokol, and Harish Vasudevan for critical reading of the manuscript. We are appreciative of Kevin Kelley and the Mouse Transgenic Core for stable tissue culture facilities. We thank the Mt. Sinai Microscopy core facility for consistent advice and top-notch instrumentation. C.J.D. was supported by F32 DE026678 from National Institutes of Health (NIH)/National Institute of Dental and Craniofacial Research (NIDCR). This work was supported by R01 DE022363 from NIH/NIDCR to P.S.

Competing Interest Statement

The authors declare no financial or non-financial competing interests.

Figure 1

Loss of Srf *in NC affects cytoskeletal gene expression*

(A) Diagram depicting SRF, its TCF and MRTF cofactors, and the upstream signals that regulate them. (B) DAPI stained embryos at E11.5 and E12.5 show a facial cleft following loss of *Srf* in NC. Scale bar represents 1mm. (C) Diagram depicting RNA-sequencing strategy. (D) Volcano plot showing DEGs in *Srf* NC conditional mutants. Genes with a p value < 0.01 and $\log_2$ fold change (FC) > 0.25 are colored. Select genes are labeled. (E) A heatmap of the top 25 DEGs by q value. The samples cluster by genotype and are color-coded by Z-score. (F) Gene set enrichment analysis (GSEA) using a list of DEGs with q ≤ 0.05 and Log2FC ≤ -0.25. Enrichment for ENCODE TF ChIP-Seq, GO Cellular Component, and GO Biological Process are shown. (G) GSEA for known SRF, MRTF, and TCF ChIP targets from previous datasets (Esnault et al., 2014; Gualdrini et al., 2016) across our entire dataset. (H) Overlap of known MRTF and TCF targets with DEGs q ≤ 0.05. (I) Absolute value of $\log_2$ FC for DEGs that overlap with each category. Horizontal bar indicates the mean (0.385 Shared, 0.378 MRTF, 0.219 TCF).

Figure 2

$Srf^{\alpha I/\alpha I}$ *embryos succumb at E10.5 with numerous defects*

(A) DAPI stained E9.5 embryos of the indicated genotypes show that compared to $Srf^{\alpha I/+}$ embryos, $Srf^{\alpha I/\alpha I}$ embryos are growth retarded, incompletely turned, have short and disorganized tails, a wavy neural tube, delayed anterior neural tube closure, and a hypoplastic or missing second pharyngeal arch (red asterisk). Scale bar represents 500 μm. (B) Brightfield images of E9.5 yolk sacs indicate defective vasculogenesis in mutant

embryos. (C) DAPI stained E10.5 embryos show more extensive growth retardation, a distended heart tube, and pericardial edema (red arrow). Scale bar represents 500 μm. (D) Immunofluorescent staining of E10.5 yolk sacs shows that mutant yolk sacs lack a remodeled vascular plexus or any large vessels. Images are representative of n=4 embryos of each genotype. Scale bar represents 250 μm. (E) Transverse sections through E10.5 embryos at the level of the heart show reduced F-actin intensity via phalloidin staining and increased non-nuclear β-Catenin levels. Images are representative of n=4 embryos of each genotype. Scale bar represents 50 μm. (F) A similar pattern Is seen in the neural tube. Scale bar represents 50 μm. (G) Cell proliferation, indicated through phospho-Histone H3 (Ser10) (pHH3) staining, is reduced in mutant embryos. Scale bar represents 50 μm. (H) Quantitation of (G), n=4 each genotype. p=0.0005, Student's unpaired two-tailed t-test. (I) Cell death, revealed through cleaved caspase 3 staining, is dramatically increased in mutant embryos. Scale bar represents 50 μm. (J) Quantitation of (I), n=3 control embryos and n=4 mutant embryos. p=0.003, Student's unpaired two-tailed t-test. Columns are the mean and error bars represent the standard deviation in (H) and (J).

Figure 3

The $Srf^{\alpha I}$ *and* Srf^{flox} *alleles exhibits similar defects in anterior mesoderm*

(A) E10.5 littermate embryos were stained with DAPI and imaged. Loss of *Srf* in the *Mesp1-Cre* lineage causes embryos to be undersized with pericardial edema, hypoplastic hearts, and turning defects. Phenotype observed in n=3/3 mutant embryos. (B) A similar experiment in which $Srf^{\alpha I}$ is the only *Srf* allele expressed in the *Mesp1-Cre* lineage. These

545 embryos appear comparable to the mutant embryos in (A), though they are clearly less
546 severely affected as they are slightly larger and partially turned. Phenotype observed in
547 n=3/3 mutant embryos. Scale bar represents 500 μm in all images. Note the 2x higher
548 crop in mutant embryos to better illustrate phenotypes.
549
550 **Figure 4**
551 *NC* Srf$^{\alpha l}$ *conditional mutants are normal at E13.5*
552 (A) DAPI stained E13.5 littermate embryos carrying a *ROSA26*$^{TdT/+}$ Cre reporter show no
553 apparent craniofacial defects in conditional mutants. Scale bar represents 500 μm. (B)
554 Diagram illustrating the culture of MEPM cells. (C) Immunofluorescent staining of
555 passage 2 MEPM cells shows reduced F-actin and SMA fluorescence in mutant cells
556 compared to cells from heterozygous littermate control embryos. Scale bar represents 50
557 μm. (D) qPCR from serum-starved and serum-stimulated MEPM cells indicates no
558 difference in IEG expression (*Egr1, Fos*) but a significant defect in *Srf* (q=0.00042 starve,
559 q=0.0095 serum), *Tagln* (q=0.00038 starve, q=0.013 serum), and *Acta2* (q=0.000011
560 starve, q=0.0027 serum) expression and a downward trend in *Vcl* expression. Values are
561 fold expression of control starved cells. N=3 control lines and n=4 mutant lines.
562 Significance was determined by Student's unpaired t-test with two-stage step-up
563 correction (Benjamini, Krieger, and Yekutieli) for multiple comparisons. Columns are the
564 mean and error bars represent the standard deviation.
565
566 **Figure 5**
567 *NC* Srf$^{\alpha l}$ *conditional mutants succumb postnatally with outflow tract defects*

(A) Kaplan-Meyer survival curve for neonatal *Srf*$^{\alpha I/flox}$*; Wnt1-Cre*$^{Tg/+}$ (Mutant) compared to littermates of all other genotypes (Control). Significance was computed at each timepoint using a Mantel-Cox log-rank test. P0 p=0.0142, P1 p<0.0001, P2 p<0.0001. (B) Stacked columns showing the distribution of PDA-related phenotypes in *Srf*$^{\alpha I/flox}$*; Wnt1-Cre*$^{Tg/+}$ neonates compared to littermates of all other genotypes. (C) DAPI-stained postnatal day 0 (P0) hearts carrying a *ROSA26*$^{Tdt/+}$ Cre lineage reporter showing the entire heart (top row) and the outflow tract region (bottom row). Examples of mutant phenotypes such as PDA, ARSA, and RAA. An asterisk indicates where the missing right subclavian artery should be. Note the ARSA mouse had succumbed prior to dissection and the image is dimmer due to the presence of clotted blood. The outflow tract defects are schematized below. Scale bar represents 500 μm. (D) Hematoxylin and eosin-stained frontal sections through P0 hearts showing mild to severe PDA and an example of VSD and PTA in mutants. Scale bar represents 500 μm. (E) Summary of our results, showing the requirements for SRF versus SRF$^{\alpha I}$ in different tissues and timepoints. A, aorta; ARSA, aberrant right subclavian artery; DA, ductus arteriosus; LCA, left common carotid artery; LSA, left subclavian artery; LV, left ventricle; P, pulmonary artery; PDA, patent ductus arteriosus; PTA, persistent truncus arteriosus; RAA, right aortic arch with mirror image branching; RCA, right common carotid artery; RSA, right subclavian artery.

Figure 1 Supplement 1

Srf *NC conditional mutants do not show early patterning defects*

E10.5 embryos subject to *in situ* hybridization using probes against *Msx1, Alx3, Six3, Shh,* and *Fgf8* showed no significant differences between *Srf* NC conditional mutants and

591 control littermates. *Msx1* embryos are shown in ¾ view to highlight maxillary expression.
592 *Fgf8* embryos are shown in frontal and profile views to highlight the ventral forebrain and
593 mandibular expression domains, respectively. Scale bar represents 500 μm.
594
595 **Figure 1 Supplement 2**
596 *Additional data related to craniofacial RNA-Seq*
597 (A) Volcano plot showing genes enriched in mandible (red) versus FNP (blue) tissue. (B)
598 Individual transcripts per million reads (TPM) values for *Hand2* and *Six3* plotted by
599 genotype, showing the expected tissue enrichment. (C) PCA plots for the individual
600 samples showing PCA1 vs PCA2 (left) and PCA1 vs PCA3 (right) indicate separation of
601 the samples by tissue (PCA1) and genotype (PCA3). Samples are color-coded by
602 genotype. (D) TPM values of *Srf* and several affected genes plotted by genotype. While
603 *Srf* levels vary somewhat among the non-clefted control genotypes, downstream targets
604 are only affected in the conditional mutants. (E) Overlap of DEGs from mandible (pink),
605 FNP (cyan), and a joint model using both tissues (yellow). (F) Enrichr GSEA for
606 upregulated genes with $q \leq 0.05$ and $Log2FC \geq 0.25$ from the joint model shows little
607 enrichment and such genes may therefore be indirect targets of SRF. (G) Enrichr GSEA
608 using a list of genes with $q \leq 0.05$ and $Log2FC \leq -0.25$ from each tissue showing similar
609 terms to the joint model, with the exception of cholesterol-related GO terms specific to the
610 FNP dataset. (H) GSEA for mandible and FNP samples compared to known SRF, MRTF,
611 and TCF targets (Esnault et al., 2014; Gualdrini et al., 2016) showing preferential
612 enrichment for MRTF targets in both datasets. Columns are the mean and error bars
613 represent the standard deviation in (B) and (D).

614

615 **Figure 2 Supplement 1**

616 *Targeting strategy and validation for* Srf^{Flag} *and* $Srf^{\alpha I}$ *alleles*

617 (A) A diagram of the targeting vector and the *Srf* locus. Homology arms containing an N-
618 terminal 3x FLAG tag with or without mutated SRF αI residues were cloned into a
619 targeting vector containing a *Pgk-NeoR* cassette flanked by loxP (I) and FRT (F)
620 sequences. Dotted lines demarcate the homology arms relative to the endogenous locus.
621 Exons are dark and UTR regions are striped. The FLAG tag is green and the location of
622 the SRF αI residues is marked by red arrowheads. Autoregulatory CarG elements at -62
623 bp, -82 bp, and +2800 bp are marked by blue asterisks. (B) Southern blot of SspI digested
624 targeted clones and WT genomic DNA blotted with the P32 labeled DNA probe indicated
625 in (A). (C) Diagram of mouse SRF protein showing the DNA-binding domain as a dark
626 box, the core MADS domain within it is labeled, subdomains are indicated underneath,
627 and the SRF αI mutations are red arrowheads. Domains are based on Zaromytidou et al.
628 (2006) with amino acid numbers adjusted for mouse. The 3x FLAG tag (not shown) was
629 inserted just downstream of the start codon.

630

631 **Figure 2 Supplement 2**

632 *SRF αI helix residues are highly conserved, but drift in clades lacking clear MRTF*
633 *homologues*

634 Representative species from major clades were subjected to BLASTP searches for
635 mouse SRF, MRTF-B, and ELK1. The presence of a reciprocal best BLASTP hit is
636 denoted in green. If a hit was negative, the search was repeated for the entire clade and

identification of a hit is represented in cyan. Negative hits for ELK1 were researched with mouse ETS1 to find any ETS domain proteins. SRF αI residues were manually inspected and divergence is denoted by the height of the green bar in 25% increments, representing the four residues. Red arrows indicate clades where the SRF αI residues diverge that are also missing readily identifiable MRTF homologs, although some of these lineages also lack TCF/ELK homologs. Blue arrows indicate clades where SRF αI residues are conserved along with presence of an MRTF homolog, but that lack an obvious TCF/ELK homolog. The asterisk indicates that although a reciprocal best BLASTP hit for MRTF-B was found in *S. rosetta*, the hit was a short protein fragment and it is unclear if it represents a true MRTF homolog. The genus *Caenorhabditis* lacks an obvious MRTF homolog, but likely MRTF homologs can be found in other nematodes such as *B. malayi*, *L. loa*, and *O. flexuosa*.

Figure 4 Supplement 1

MRTF-A translocates to the nucleus normally in response to serum stimulation in mutant MEPM cells

(A) Serum starved or stimulated P2 primary MEPM cells from *Srf*$^{\alpha I/flox}$*; Wnt1-Cre*$^{Tg/+}$*; ROSA26*$^{TdT/+}$ (mutant) and *Srf*$^{flox/+}$*; Wnt1-Cre*$^{Tg/+}$*; ROSA26*$^{TdT/+}$ (control) embryos were stained for MRTF-A and DAPI. (B) Nuclear MRTF-A levels were quantified using the DAPI channel to identify nuclei. Dots represent individual cells pooled from n=2 unique cell lines for each genotype. Horizontal bars are the mean and error bars represent the standard deviation.

Figure 5 Supplement 1

E18.5 conditional mutant skulls are delayed but correctly patterned

Alizarin red (bone) and alcian blue (cartilage) stained E18.5 skulls of the indicated genotypes from two litters are shown. All three conditional mutant embryos were smaller than their control littermates and had less extensive ossification. However, all the indicated bones were present in each genotype, except for the presphenoid bone, which was missing in 2/3 mutants (location of missing bone indicated in bold) and rudimentary in one (italics). Bo, basioccipital; bs, basisphenoid; eo, exoccipital; etm, ectotympanic; fmx, frontal process of maxilla; fr, frontal; h, hyoid; ip, interparietal; jg, jugal; m, mandible; mx, maxilla; na, nasal; pl, palatine; pmx, premaxilla; ppmx, palatal process of maxilla; pppl, palatal process of palatine; pppmx, palatal process of premaxilla; pr, parietal; ps, presphenoid; ptg, pterygoid; rtp, retrotympanic process; so, supraoccipital; sq, squamosal; zpmx, zygomatic process of maxilla.

Figure 5 Supplement 2

Pdgfra *and* Srf$^{\alpha l}$ *do not interact genetically in NC*

(A) Expected and recovered numbers of embryos of each genotype at birth (P0). No significant deviation from Mendelian ratios was observed. (B) PDA-related phenotypes in *Srf$^{\alpha l/flox}$; Wnt1-Cre$^{Tg/+}$* neonates are not exacerbated by the loss of one copy of *Pdgfra*.

Table 1

Srf$^{\alpha l/\alpha l}$ *embryos are not recovered at weaning*

Expected and recovered numbers of embryos of each genotype at weaning (P21). No homozygous mutant embryos were recovered.

Reaction	Primer 1	Primer 2	Primer 3	Primer 4	WT Product	Mutant Product
Srf^{flox}	TGCTTACTGGAAAGCTCATGG	TGCTGGTTTGGCATCAACT			210 bp	430 bp
Srf^{-}	GCTTACTGGAAAGCTCATGG	CTAACCCTGCCTGTCCTTCA				475 bp
Srf^{FLAG}, *Srf$^{\alpha I}$*	GATGAACGATGTGACCTCGC	AGGGAGGAGCCAACTCCTTA			347 bp	467 bp
Pdgfra$^{H2B-EGFP}$	CCCTTGTGGTCATGCCAAAC	GCTTTTGCCTCCATTACACTGG	ACGAAGTTATTAGGTCCCTCGAC		451 bp	242 bp
Cre	GCTGCCACGACCAAGTGACAGCAATG	GTAGTTATTCGGATCATCAGCTACAC				400 bp
MORE-Cre	GGGACCACCTTCTTTTGGCTTC	AAGATGTGGAGAGTTCGGGGTAG	CCAGATCCTCCTCAGAAATCAGC		411 bp	311 bp
ROSA26^{mTmG}	CTCTGCTGCCTCCTGGCTTCT	CGAGGCGGATCACAAGCAATA	TCAATGGGCGGGGGTCGTT		330 bp	250 bp
ROSA26^{TdT}	AAGGGAGCTGCAGTGGAGTA	CCGAAAATCTGTGGGAAGTC	GGCATTAAAGCAGCGTATCC	CTGTTCCTGTACGGCATGG	297 bp	196 bp

Supplementary Table 1

Genotyping Primers

A list of genotyping primers and product sizes. All reactions were run for 35 cycles with an annealing temperature of 60º C.

Gene	Forward Primer	Reverse Primer	cDNA amplicon	Genomic amplicon
Acta2	GGCACCACTGAACCCTAAGG	ACAATACCAGTTGTACGTCCAGA	135 bp	1822 bp
Egr1	TGGGATAACTCGTCTCCACC	GAGCGAACAACCCTATGAGC	92 bp	770 bp
Fos	TCCTACTACCATTCCCCAGC	TGGCACTAGAGACGGACAGA	94 bp	848 bp
Hprt	TCCTCCTCAGACCGCTTTT	CATAACCTGGTTCATCATCGC	95 bp	10935 bp
Srf	GTGCCACTGGCTTTGAAGA	GCAGGTTGGTGACTGTGAAT	108 bp	1875 bp
Tagln	GACTGCACTTCTCGGCTCAT	CCGAAGCTACTCTCCTTCCA	100 bp	4160 bp
Vcl	TCTGATCCTCAGTGGTCTGAAC	AAAGCCATTCCTGACCTCAC	103 bp	41200 bp

692 **Supplementary Table 2**

693 *qPCR Primers*

694 Forward and reverse primer sequences used for qPCR experiments in Figure 4D. All
695 primers are listed 5' to 3'.

696

697 **Supplementary File 1**

698 *RNA-Seq gene lists*

699 A Microsoft Excel file containing gene expression analysis for the mandible, FNP, and
700 joint mandible+FNP datasets, gene lists used to generate Figure 1G-H, raw counts and
701 TPM values for each sample, and the variables used for each sample to classify it for
702 analysis in Sleuth: genotype, tissue, and litter.

703

Materials and Methods

Animal Husbandry

All animal experimentation was conducted according to protocols approved by the Institutional Animal Care and Use Committee of the Icahn School of Medicine at Mount Sinai. Mice were kept in a dedicated animal vivarium with veterinarian support. They were housed on a 13hr-11hr light-dark cycle and had access to food and water *ad libitum*.

Mouse Models

The following previously described mouse lines were used: *H2az2*$^{Tg(wnt1\text{-}cre)11Rth}$ referred to as *Wnt1-Cre* (Danielian et al., 1998), *Mesp1*$^{tm2(cre)Ysa}$ referred to as *Mesp1*^{Cre} (Saga et al., 1999), *Srf*^{tm1Rmn} referred to as *Srf*^{flox} (Miano et al., 2004), *Meox2*$^{tm1(cre)Sor}$ referred to as *MORE-Cre* (Tallquist & Soriano, 2000), *Gt(ROSA)26Sor*$^{tm14(CAG\text{-}TdTomato)Hze}$ referred to as *R26R*^{TdT} (Madisen et al., 2010), and *Gt(ROSA)26Sor*$^{tm4(ACTB\text{-}tdTomato,\text{-}EGFP)Luo}$ referred to as *R26R*^{mTmG} (Muzumdar et al., 2007). *Srf*^{FLAG} and *Srf*$^{\alpha I}$ mice were generated by gene targeting. Homology arms of 2kb and 6.4kb were cloned into the pPGKneoF2L2DTA backbone. The longer arm was assembled in three fragments using HiFi assembly cloning (NEB) and included a 3x FLAG tag introduced with a primer. Fragments were amplified from 129S4 gDNA using Q5 polymerase (NEB) except for the middle segment of the long arm (i.e. the coding sequence of exon 1), which was amplified from a cDNA clone before or after introducing the αI helix mutations via site-directed mutagenesis. The targeting constructs were linearized and electroporated in AK7 (129S4 lineage) embryonic stem cells. Clones were selected with G418, screened by long-range PCR, and verified by Southern blot. Correctly targeted clones were injected into C57BL6/J E3.5

727 blastocysts, transferred to pseudopregnant F1 (C57BL6/J X 129S4) surrogates, and
728 chimeras selected based on coat color. Founders were crossed to *MORE-Cre* mice to
729 remove the *NeoR* cassette (Tallquist & Soriano, 2000). All mice were analyzed on a
730 129S4 co-isogenic background. Genotyping primers are available in Supplementary
731 Table 1.
732
733 *Conservation*
734 Representative species from the various taxa were subject to BLASTP searches with
735 default parameters using the amino acid sequences for mouse SRF, MKL2, and ELK1.
736 Potential hits were then confirmed by reciprocal BLASTP back to mouse. If a species
737 lacked an ELK1 homolog, the mouse ETS1 sequence was used to search for ETS-
738 domain containing genes. If the given species lacked a hit for a particular search, the
739 search was repeated for the entire taxon. Ctenophora were searched using amino acid
740 sequences for mouse SRF and MEF2C, yeast MCM2, snapdragon Deficiens, and
741 Arabidopsis Agamous. No homolog was identified, suggesting loss of MADS proteins in
742 this lineage.
743
744 *RNA Sequencing*
745 FNPs (LNP + MNP) and mandibles were carefully removed from E11.5 embryos in ice-
746 cold PBS using fine forceps. A total of eight embryos across two litters representing four
747 mutants and four controls were collected. Total RNA was immediately extracted using the
748 RNeasy Plus Mini kit (Qiagen). RNA quality was assessed by Tapestation and all samples

had RIN scores ≥ 9.8. Samples were sent to GeneWiz for PE150 sequencing. There were 14.6-30m reads / sample and an average of 24.2m reads / sample.

Reads were pseudo-aligned to the mouse transcriptome (mm10 partial selective alignment method, downloaded from refgenie) using salmon 1.5.0 and the flags –validateMappings –gcBias –numBootstraps 30. Pseudoalignments were processed with wasabi 1.0.1 and analyzed with sleuth 0.30.0-4 with the flag gene_mode=true. Analysis was performed using a full model that accounted for genotype, litter/batch, and tissue-of-origin (for combined tissue analysis only) versus a reduced model consisting only of litter/batch (and tissue-of-origin). Fold-changes and q-values were computed using the Wald test. Volcano plots were made with VolcaNoseR. Heat maps were generated using the Shinyapp HeatMappr. Gene set enrichment analysis for GO terms, ENCODE datasets, etc. were done with the web utility Enrichr (Xie et al., 2021). Enrichment for a custom list of targets was performed using GSEA software 4.10 and normalized read counts for the entire dataset. Analysis for the joint tissue model was run in phenotype mode (>7 samples per condition) and for the individual tissue samples in gene_set mode (<7 samples per condition) according to the software developer. The maximum number of genes per set was raised to 800 to accommodate the target lists. All other parameters were default.

MEPM Culture

Mouse embryonic palatal mesenchyme cells were generated as described (Fantauzzo & Soriano, 2017). Briefly, palatal shelves were dissected from E13.5 embryos in ice cold

PBS using fine forceps. Yolk sac tissue was used for genotyping. Palates from individual embryos were held on ice until dissection was complete and palates were then dissociated using 0.125% Trypsin-EDTA at 37º C for 10 minutes with occasional trituration using a P1000 pipet. Trypsin was neutralized with an equal volume of growth media (DMEM High Glucose supplemented with Glutamine, Penicillin-Streptomycin, and 10% Fetal Calf III serum) and plated onto culture dishes coated in 0.1% gelatin. Cells were passaged as they approached confluency, every 2-3 days, and used for experiments at passage 2.

Immunofluorescence

MEPM cells were seeded on #1.5 coverslips coated with 0.1% gelatin. For starvation experiments, cells were starved overnight in 0.1% serum then stimulated 30' with 10% serum. Cells were fixed using 4% PFA in PBS for 10' at 37º C. Embryos were dissected in ice cold PBS, fixed one hour in 4% PFA in PBS at 4º C, rinsed in PBS, cryoprotected in 30% sucrose, and embedded in OCT. Sections were cut at 10 um thickness using a Leica cryostat. Yolk sacs were fixed one hour in 4% PFA in PBS at 4º C and stained whole. All samples were rinsed in PBS, blocked and permeabilized in blocking media (PBS, 0.3% TritonX-100, 1% BSA, 5% calf serum) one hour at RT, primary antibody was diluted in fresh blocking media and samples treated overnight at 4º C, washed 3x PBS at RT, incubated in Alexa Fluor Plus-conjugated secondary antibodies (Invitrogen) diluted 1:500 in fresh blocking media with 1 μg/ml DAPI for 1-2 hours at RT or overnight at 4º C, and finally washed 3x in PBS at RT. Samples were mounted in Prolong Diamond (Invitrogen) mounting media and imaged on a Zeiss AxioObserver inverted fluorescence

795 microscope or a Zeiss 780 upright confocal microscope. Thresholding was performed and
796 scalebars added in the FIJI implementation of ImageJ. All images for a given experiment
797 were processed identically.
798
799 Quantitation of cell proliferation and cell death was performed by staining frozen sections
800 with the indicated antibodies. Sections at the level of the heart were imaged using a 10x
801 objective on a Zeiss 780 confocal microscope, a 1024x1024 pixel count and 6 um step
802 size. Tiling was used with 10% overlap when necessary to image the entire section.
803 Maximum intensity projections were made in the FIJI implementation of ImageJ and
804 identical thresholds used for each embryo to calculate the DAPI-positive and cleaved
805 Caspase 3-positive or phospho-Histone H3 (Ser 10)-positive area on sections at the level
806 of the heart. Any of the embryo's posterior present in the section was ignored as this
807 region was not present in all sections for all embryos.
808
809 Antibodies used were rabbit anti β-Catenin (Cell Signaling, 8480) 1:200, rat anti-CD31
810 (BD Pharmingen, 553370) 1:50, rabbit anti-cleaved Caspase 3 (Cell Signaling 9665,
811 1:400), rabbit anti-phospho Histone H3 (Ser10) (Millipore 06-570, 1:500), rabbit anti-
812 MKL1 (Proteintech, 21166-1-AP) 1:100, rabbit anti-SMA (Cell Signaling, 19245) 1:200.
813 Phalloidin-Alexa Fluor 647 (Invitrogen) was included where indicated during secondary
814 antibody staining at 1:400.
815
816 *RT-qPCR*

Cells were seeded, passaged, starved, and stimulated as for immunofluorescence except in 12-well tissue culture plates. Embryo facial prominences were dissected in cold PBS and transferred to 1.5 ml microfuge tubes on ice. Following the indicated stimulation regimes when applicable, cells/tissue were lysed in 300 μl RLT buffer supplemented with BME, and RNA isolated using the RNeasy Plus Kit (Qiagen) according to the manufacturer's instructions. RNA concentration was quantified using a Nanodrop. 1 μg total RNA was used for reverse transcription. RNA was primed using a 2:1 molar ratio of random hexamer and polydT (Invitrogen) and reverse transcribed with Superscript IV (Invitrogen) according to the manufacture's protocol. Resulting cDNA was diluted 5x with water and stored at -20º C. 1 μl cDNA was used per qPCR reaction. qPCR was performed using Luna 2x Master Mix (NEB) on an iQ5 thermocycler (Bio-Rad) in triplicate. Differences in gene expression were calculated by ΔΔCT using *Hprt* for normalization. Primer sequences are listed in Supplementary Table 2.

Nuclear Translocation Analysis

Cells were starved, treated, and stained as described above and imaged on an inverted Zeiss AxioObserver microscope. Z-stacks were maximum intensity projected in the FIJI implementation of ImageJ, background subtracted, and the DAPI channel used to create a nuclear mask. This mask was then used to measure the average nuclear intensity in the MRTF-A channel for each nucleus. The data presented are the pooled results from 2 cell lines of each genotype where each dot is an individual nucleus. At least 70 cells were analyzed per condition.

In situ hybridization

E10.5 embryos were dissected in ice-cold PBS and fixed overnight in 4% FA in PBS at 4º C, rinsed in PBS, dehydrated through a MeOH series and stored in 100% MeOH at -20º C. Embryos were stained using standard techniques for the indicated transcripts using published, DIG-labeled probes, and were developed in BM Purple (Roche | Sigma-Aldrich). For *Fgf8* the proteinase-K digestion was omitted in order to maintain integrity of the ectoderm. Probe sequences and a detailed protocol are available upon request.

Histology

P0 hearts were fixed overnight in 4% FA in PBS at 4º C, rinsed in PBS, dehydrated through an ethanol series, and embedded in paraffin. 5 μm sections were cut using a Leica microtome. After drying, sections were stained with Harris modified hematoxylin (Fisher) and Eosin Y using a standard regressive staining protocol.

Skeletal Preparations

Skeletons were stained by standard techniques. Briefly, E18.5 embryos were skinned, eviscerated, fixed in ethanol, stained with .015% alcian blue and .005% alizarin red overnight at 37º C, cleared in 1% KOH, processed through a glycerol:KOH series, and photographed in 80% glycerol in PBS.

Statistical Methods

Specific statistical methods, significance values, and n are detailed in the figure legends. For RNA-Seq, statistics were computed using the built-in Wald Test function in the Sleuth analysis package. All other statistics were performed using GraphPad Prism 9.

Data Availability

Processed and raw RNA-Seq files have been deposited in the Gene Expression Omnibus under the accession number GSE186770.

References

Arsenian, S., Weinhold, B., Oelgeschlager, M., Ruther, U., & Nordheim, A. (1998). Serum response factor is essential for mesoderm formation during mouse embryogenesis. *EMBO J*, *17*(21), 6289-6299. https://doi.org/10.1093/emboj/17.21.6289

Asparuhova, M. B., Ferralli, J., Chiquet, M., & Chiquet-Ehrismann, R. (2011). The transcriptional regulator megakaryoblastic leukemia-1 mediates serum response factor-independent activation of tenascin-C transcription by mechanical stress. *FASEB J*, *25*(10), 3477-3488. https://doi.org/10.1096/fj.11-187310

Ayadi, A., Zheng, H., Sobieszczuk, P., Buchwalter, G., Moerman, P., Alitalo, K., & Wasylyk, B. (2001). Net-targeted mutant mice develop a vascular phenotype and up-regulate egr-1. *EMBO J*, *20*(18), 5139-5152. https://doi.org/10.1093/emboj/20.18.5139

Belaguli, N. S., Sepulveda, J. L., Nigam, V., Charron, F., Nemer, M., & Schwartz, R. J. (2000). Cardiac tissue enriched factors serum response factor and GATA-4 are mutual coregulators. *Mol Cell Biol*, *20*(20), 7550-7558. https://doi.org/10.1128/MCB.20.20.7550-7558.2000

Bergwerff, M., Gittenberger-de Groot, A. C., Wisse, L. J., DeRuiter, M. C., Wessels, A., Martin, J. F., Olson, E. N., & Kern, M. J. (2000). Loss of function of the Prx1 and Prx2 homeobox genes alters architecture of the great elastic arteries and ductus arteriosus. *Virchows Arch*, *436*(1), 12-19. https://doi.org/10.1007/pl00008193

Brachmann, S. M., Yballe, C. M., Innocenti, M., Deane, J. A., Fruman, D. A., Thomas, S. M., & Cantley, L. C. (2005). Role of phosphoinositide 3-kinase regulatory isoforms in development and actin rearrangement. *Mol Cell Biol*, *25*(7), 2593-2606. https://doi.org/10.1128/MCB.25.7.2593-2606.2005

Brewer, J. R., Molotkov, A., Mazot, P., Hoch, R. V., & Soriano, P. (2015). Fgfr1 regulates development through the combinatorial use of signaling proteins. *Genes Dev*, *29*(17), 1863-1874. https://doi.org/10.1101/gad.264994.115

Bronner, M. E., & Simoes-Costa, M. (2016). The Neural Crest Migrating into the Twenty-First Century. *Curr Top Dev Biol*, *116*, 115-134. https://doi.org/10.1016/bs.ctdb.2015.12.003

Cenik, B. K., Liu, N., Chen, B., Bezprozvannaya, S., Olson, E. N., & Bassel-Duby, R. (2016). Myocardin-related transcription factors are required for skeletal muscle development. *Development*, *143*(15), 2853-2861. https://doi.org/10.1242/dev.135855

Cesari, F., Rennekampff, V., Vintersten, K., Vuong, L. G., Seibler, J., Bode, J., Wiebel, F. F., & Nordheim, A. (2004). Elk-1 knock-out mice engineered by Flp recombinase-mediated cassette exchange. *Genesis*, *38*(2), 87-92. https://doi.org/10.1002/gene.20003

Chen, C. Y., Croissant, J., Majesky, M., Topouzis, S., McQuinn, T., Frankovsky, M. J., & Schwartz, R. J. (1996). Activation of the cardiac alpha-actin promoter depends upon serum response factor, Tinman homologue, Nkx-2.5, and intact serum response elements. *Dev Genet*, *19*(2), 119-130. https://doi.org/10.1002/(SICI)1520-6408(1996)19:2<119::AID-DVG3>3.0.CO;2-C

Chen, F., Kook, H., Milewski, R., Gitler, A. D., Lu, M. M., Li, J., Nazarian, R., Schnepp, R., Jen, K., Biben, C., Runke, G., Mackay, J. P., Novotny, J., Schwartz, R. J., Harvey, R. P., Mullins, M. C., & Epstein, J. A. (2002). Hop is an unusual homeobox gene that modulates cardiac development. *Cell*, *110*(6), 713-723. https://doi.org/10.1016/s0092-8674(02)00932-7

911 Costello, P., Nicolas, R., Willoughby, J., Wasylyk, B., Nordheim, A., & Treisman, R. (2010).
912 Ternary complex factors SAP-1 and Elk-1, but not net, are functionally equivalent in
913 thymocyte development. *J Immunol*, *185*(2), 1082-1092.
914 https://doi.org/10.4049/jimmunol.1000472
915 Costello, P. S., Nicolas, R. H., Watanabe, Y., Rosewell, I., & Treisman, R. (2004). Ternary complex
916 factor SAP-1 is required for Erk-mediated thymocyte positive selection. *Nat Immunol*,
917 *5*(3), 289-298. https://doi.org/10.1038/ni1038
918 Creemers, E. E., Sutherland, L. B., Oh, J., Barbosa, A. C., & Olson, E. N. (2006). Coactivation of
919 MEF2 by the SAP domain proteins myocardin and MASTR. *Mol Cell*, *23*(1), 83-96.
920 https://doi.org/10.1016/j.molcel.2006.05.026
921 Danielian, P. S., Muccino, D., Rowitch, D. H., Michael, S. K., & McMahon, A. P. (1998).
922 Modification of gene activity in mouse embryos in utero by a tamoxifen-inducible form
923 of Cre recombinase. *Curr Biol*, *8*(24), 1323-1326. https://doi.org/10.1016/s0960-
924 9822(07)00562-3
925 Dinsmore, C. J., & Soriano, P. (2018). MAPK and PI3K signaling: At the crossroads of neural crest
926 development. *Dev Biol*, *444 Suppl 1*, S79-S97.
927 https://doi.org/10.1016/j.ydbio.2018.02.003
928 Enkhmandakh, B., Makeyev, A. V., Erdenechimeg, L., Ruddle, F. H., Chimge, N. O., Tussie-Luna,
929 M. I., Roy, A. L., & Bayarsaihan, D. (2009). Essential functions of the Williams-Beuren
930 syndrome-associated TFII-I genes in embryonic development. *Proc Natl Acad Sci U S A*,
931 *106*(1), 181-186. https://doi.org/10.1073/pnas.0811531106
932 Esnault, C., Gualdrini, F., Horswell, S., Kelly, G., Stewart, A., East, P., Matthews, N., & Treisman,
933 R. (2017). ERK-Induced Activation of TCF Family of SRF Cofactors Initiates a Chromatin
934 Modification Cascade Associated with Transcription. *Mol Cell*, *65*(6), 1081-1095 e1085.
935 https://doi.org/10.1016/j.molcel.2017.02.005
936 Esnault, C., Stewart, A., Gualdrini, F., East, P., Horswell, S., Matthews, N., & Treisman, R. (2014).
937 Rho-actin signaling to the MRTF coactivators dominates the immediate transcriptional
938 response to serum in fibroblasts. *Genes Dev*, *28*(9), 943-958.
939 https://doi.org/10.1101/gad.239327.114
940 Espinoza-Lewis, R. A., & Wang, D. Z. (2014). Generation of a Cre knock-in into the Myocardin
941 locus to mark early cardiac and smooth muscle cell lineages. *Genesis*, *52*(10), 879-887.
942 https://doi.org/10.1002/dvg.22819
943 Fantauzzo, K. A., & Soriano, P. (2015). Receptor tyrosine kinase signaling: regulating neural crest
944 development one phosphate at a time. *Curr Top Dev Biol*, *111*, 135-182.
945 https://doi.org/10.1016/bs.ctdb.2014.11.005
946 Fantauzzo, K. A., & Soriano, P. (2017). Generation of an immortalized mouse embryonic palatal
947 mesenchyme cell line. *PLoS One*, *12*(6), e0179078.
948 https://doi.org/10.1371/journal.pone.0179078
949 Feng, Y., Chen, M. H., Moskowitz, I. P., Mendonza, A. M., Vidali, L., Nakamura, F., Kwiatkowski,
950 D. J., & Walsh, C. A. (2006). Filamin A (FLNA) is required for cell-cell contact in vascular
951 development and cardiac morphogenesis. *Proc Natl Acad Sci U S A*, *103*(52), 19836-
952 19841. https://doi.org/10.1073/pnas.0609628104
953 Fox, J. W., Lamperti, E. D., Eksioglu, Y. Z., Hong, S. E., Feng, Y., Graham, D. A., Scheffer, I. E.,
954 Dobyns, W. B., Hirsch, B. A., Radtke, R. A., Berkovic, S. F., Huttenlocher, P. R., & Walsh,

C. A. (1998). Mutations in filamin 1 prevent migration of cerebral cortical neurons in human periventricular heterotopia. *Neuron*, *21*(6), 1315-1325. https://doi.org/10.1016/s0896-6273(00)80651-0

Freddie, C. T., Ji, Z., Marais, A., & Sharrocks, A. D. (2007). Functional interactions between the Forkhead transcription factor FOXK1 and the MADS-box protein SRF. *Nucleic Acids Res*, *35*(15), 5203-5212. https://doi.org/10.1093/nar/gkm528

Grueneberg, D. A., Henry, R. W., Brauer, A., Novina, C. D., Cheriyath, V., Roy, A. L., & Gilman, M. (1997). A multifunctional DNA-binding protein that promotes the formation of serum response factor/homeodomain complexes: identity to TFII-I. *Genes Dev*, *11*(19), 2482-2493. https://doi.org/10.1101/gad.11.19.2482

Grueneberg, D. A., Natesan, S., Alexandre, C., & Gilman, M. Z. (1992). Human and Drosophila homeodomain proteins that enhance the DNA-binding activity of serum response factor. *Science*, *257*(5073), 1089-1095. https://doi.org/10.1126/science.257.5073.1089

Gualdrini, F., Esnault, C., Horswell, S., Stewart, A., Matthews, N., & Treisman, R. (2016). SRF Co-factors Control the Balance between Cell Proliferation and Contractility. *Mol Cell*, *64*(6), 1048-1061. https://doi.org/10.1016/j.molcel.2016.10.016

Guo, B., Lyu, Q., Slivano, O. J., Dirkx, R., Christie, C. K., Czyzyk, J., Hezel, A. F., Gharavi, A. G., Small, E. M., & Miano, J. M. (2018). Serum Response Factor Is Essential for Maintenance of Podocyte Structure and Function. *J Am Soc Nephrol*, *29*(2), 416-422. https://doi.org/10.1681/ASN.2017050473

Hanna, S., & El-Sibai, M. (2013). Signaling networks of Rho GTPases in cell motility. *Cell Signal*, *25*(10), 1955-1961. https://doi.org/10.1016/j.cellsig.2013.04.009

Hipp, L., Beer, J., Kuchler, O., Reisser, M., Sinske, D., Michaelis, J., Gebhardt, J. C. M., & Knoll, B. (2019). Single-molecule imaging of the transcription factor SRF reveals prolonged chromatin-binding kinetics upon cell stimulation. *Proc Natl Acad Sci U S A*, *116*(3), 880-889. https://doi.org/10.1073/pnas.1812734116

Houweling, A. C., Beaman, G. M., Postma, A. V., Gainous, T. B., Lichtenbelt, K. D., Brancati, F., Lopes, F. M., van der Made, I., Polstra, A. M., Robinson, M. L., Wright, K. D., Ellingford, J. M., Jackson, A. R., Overwater, E., Genesio, R., Romano, S., Camerota, L., D'Angelo, E., Meijers-Heijboer, E. J., Christoffels, V. M., McHugh, K. M., Black, B. L., Newman, W. G., Woolf, A. S., & Creemers, E. E. (2019). Loss-of-function variants in myocardin cause congenital megabladder in humans and mice. *J Clin Invest*, *129*(12), 5374-5380. https://doi.org/10.1172/JCI128545

Huang, J., Cheng, L., Li, J., Chen, M., Zhou, D., Lu, M. M., Proweller, A., Epstein, J. A., & Parmacek, M. S. (2008). Myocardin regulates expression of contractile genes in smooth muscle cells and is required for closure of the ductus arteriosus in mice. *J Clin Invest*, *118*(2), 515-525. https://doi.org/10.1172/JCI33304

Jimenez, C., Portela, R. A., Mellado, M., Rodriguez-Frade, J. M., Collard, J., Serrano, A., Martinez, A. C., Avila, J., & Carrera, A. C. (2000). Role of the PI3K regulatory subunit in the control of actin organization and cell migration. *J Cell Biol*, *151*(2), 249-262. https://doi.org/10.1083/jcb.151.2.249

Kim, D. W., Cheriyath, V., Roy, A. L., & Cochran, B. H. (1998). TFII-I enhances activation of the c-fos promoter through interactions with upstream elements. *Mol Cell Biol*, *18*(6), 3310-3320. https://doi.org/10.1128/MCB.18.6.3310

Kim, T., Hwang, D., Lee, D., Kim, J. H., Kim, S. Y., & Lim, D. S. (2017). MRTF potentiates TEAD-YAP transcriptional activity causing metastasis. *EMBO J*, *36*(4), 520-535. https://doi.org/10.15252/embj.201695137

Lemmon, M. A., & Schlessinger, J. (2010). Cell signaling by receptor tyrosine kinases. *Cell*, *141*(7), 1117-1134. https://doi.org/10.1016/j.cell.2010.06.011

Li, J., Bowens, N., Cheng, L., Zhu, X., Chen, M., Hannenhalli, S., Cappola, T. P., & Parmacek, M. S. (2012). Myocardin-like protein 2 regulates TGFbeta signaling in embryonic stem cells and the developing vasculature. *Development*, *139*(19), 3531-3542. https://doi.org/10.1242/dev.082222

Li, J., Zhu, X., Chen, M., Cheng, L., Zhou, D., Lu, M. M., Du, K., Epstein, J. A., & Parmacek, M. S. (2005). Myocardin-related transcription factor B is required in cardiac neural crest for smooth muscle differentiation and cardiovascular development. *Proc Natl Acad Sci U S A*, *102*(25), 8916-8921. https://doi.org/10.1073/pnas.0503741102

Li, S., Chang, S., Qi, X., Richardson, J. A., & Olson, E. N. (2006). Requirement of a myocardin-related transcription factor for development of mammary myoepithelial cells. *Mol Cell Biol*, *26*(15), 5797-5808. https://doi.org/10.1128/MCB.00211-06

Li, S., Czubryt, M. P., McAnally, J., Bassel-Duby, R., Richardson, J. A., Wiebel, F. F., Nordheim, A., & Olson, E. N. (2005). Requirement for serum response factor for skeletal muscle growth and maturation revealed by tissue-specific gene deletion in mice. *Proc Natl Acad Sci U S A*, *102*(4), 1082-1087. https://doi.org/10.1073/pnas.0409103102

Li, S., Wang, D. Z., Wang, Z., Richardson, J. A., & Olson, E. N. (2003). The serum response factor coactivator myocardin is required for vascular smooth muscle development. *Proc Natl Acad Sci U S A*, *100*(16), 9366-9370. https://doi.org/10.1073/pnas.1233635100

Liu, Z. P., Wang, Z., Yanagisawa, H., & Olson, E. N. (2005). Phenotypic modulation of smooth muscle cells through interaction of Foxo4 and myocardin. *Dev Cell*, *9*(2), 261-270. https://doi.org/10.1016/j.devcel.2005.05.017

Lu, M. F., Cheng, H. T., Kern, M. J., Potter, S. S., Tran, B., Diekwisch, T. G., & Martin, J. F. (1999). prx-1 functions cooperatively with another paired-related homeobox gene, prx-2, to maintain cell fates within the craniofacial mesenchyme. *Development*, *126*(3), 495-504. https://www.ncbi.nlm.nih.gov/pubmed/9876178

Madisen, L., Zwingman, T. A., Sunkin, S. M., Oh, S. W., Zariwala, H. A., Gu, H., Ng, L. L., Palmiter, R. D., Hawrylycz, M. J., Jones, A. R., Lein, E. S., & Zeng, H. (2010). A robust and high-throughput Cre reporting and characterization system for the whole mouse brain. *Nat Neurosci*, *13*(1), 133-140. https://doi.org/10.1038/nn.2467

Mengmeng, X., Yuejuan, X., Sun, C., Yanan, L., Fen, L., & Kun, S. (2020). Novel mutations of the SRF gene in Chinese sporadic conotruncal heart defect patients. *BMC Med Genet*, *21*(1), 95. https://doi.org/10.1186/s12881-020-01032-y

Miano, J. M. (2003). Serum response factor: toggling between disparate programs of gene expression. *J Mol Cell Cardiol*, *35*(6), 577-593. https://doi.org/10.1016/s0022-2828(03)00110-x

Miano, J. M., Ramanan, N., Georger, M. A., de Mesy Bentley, K. L., Emerson, R. L., Balza, R. O., Jr., Xiao, Q., Weiler, H., Ginty, D. D., & Misra, R. P. (2004). Restricted inactivation of serum response factor to the cardiovascular system. *Proc Natl Acad Sci U S A*, *101*(49), 17132-17137. https://doi.org/10.1073/pnas.0406041101

Minoux, M., Holwerda, S., Vitobello, A., Kitazawa, T., Kohler, H., Stadler, M. B., & Rijli, F. M. (2017). Gene bivalency at Polycomb domains regulates cranial neural crest positional identity. *Science*, *355*(6332). https://doi.org/10.1126/science.aal2913

Miralles, F., Posern, G., Zaromytidou, A. I., & Treisman, R. (2003). Actin dynamics control SRF activity by regulation of its coactivator MAL. *Cell*, *113*(3), 329-342. https://doi.org/10.1016/s0092-8674(03)00278-2

Mohun, T. J., Chambers, A. E., Towers, N., & Taylor, M. V. (1991). Expression of genes encoding the transcription factor SRF during early development of Xenopus laevis: identification of a CArG box-binding activity as SRF. *EMBO J*, *10*(4), 933-940. https://www.ncbi.nlm.nih.gov/pubmed/2009862

Morin, S., Paradis, P., Aries, A., & Nemer, M. (2001). Serum response factor-GATA ternary complex required for nuclear signaling by a G-protein-coupled receptor. *Mol Cell Biol*, *21*(4), 1036-1044. https://doi.org/10.1128/MCB.21.4.1036-1044.2001

Muzumdar, M. D., Tasic, B., Miyamichi, K., Li, L., & Luo, L. (2007). A global double-fluorescent Cre reporter mouse. *Genesis*, *45*(9), 593-605. https://doi.org/10.1002/dvg.20335

Mylona, A., Theillet, F. X., Foster, C., Cheng, T. M., Miralles, F., Bates, P. A., Selenko, P., & Treisman, R. (2016). Opposing effects of Elk-1 multisite phosphorylation shape its response to ERK activation. *Science*, *354*(6309), 233-237. https://doi.org/10.1126/science.aad1872

Newbern, J., Zhong, J., Wickramasinghe, R. S., Li, X., Wu, Y., Samuels, I., Cherosky, N., Karlo, J. C., O'Loughlin, B., Wikenheiser, J., Gargesha, M., Doughman, Y. Q., Charron, J., Ginty, D. D., Watanabe, M., Saitta, S. C., Snider, W. D., & Landreth, G. E. (2008). Mouse and human phenotypes indicate a critical conserved role for ERK2 signaling in neural crest development. *Proc Natl Acad Sci U S A*, *105*(44), 17115-17120. https://doi.org/10.1073/pnas.0805239105

Niu, Z., Yu, W., Zhang, S. X., Barron, M., Belaguli, N. S., Schneider, M. D., Parmacek, M., Nordheim, A., & Schwartz, R. J. (2005). Conditional mutagenesis of the murine serum response factor gene blocks cardiogenesis and the transcription of downstream gene targets. *J Biol Chem*, *280*(37), 32531-32538. https://doi.org/10.1074/jbc.M501372200

Norman, C., Runswick, M., Pollock, R., & Treisman, R. (1988). Isolation and properties of cDNA clones encoding SRF, a transcription factor that binds to the c-fos serum response element. *Cell*, *55*(6), 989-1003. https://doi.org/10.1016/0092-8674(88)90244-9

Oh, J., Richardson, J. A., & Olson, E. N. (2005). Requirement of myocardin-related transcription factor-B for remodeling of branchial arch arteries and smooth muscle differentiation. *Proc Natl Acad Sci U S A*, *102*(42), 15122-15127. https://doi.org/10.1073/pnas.0507346102

Panayiotou, R., Miralles, F., Pawlowski, R., Diring, J., Flynn, H. R., Skehel, M., & Treisman, R. (2016). Phosphorylation acts positively and negatively to regulate MRTF-A subcellular localisation and activity. *Elife*, *5*. https://doi.org/10.7554/eLife.15460

Parlakian, A., Tuil, D., Hamard, G., Tavernier, G., Hentzen, D., Concordet, J. P., Paulin, D., Li, Z., & Daegelen, D. (2004). Targeted inactivation of serum response factor in the developing heart results in myocardial defects and embryonic lethality. *Mol Cell Biol*, *24*(12), 5281-5289. https://doi.org/10.1128/MCB.24.12.5281-5289.2004

Parmacek, M. S. (2007). Myocardin-related transcription factors: critical coactivators regulating cardiovascular development and adaptation. *Circ Res*, *100*(5), 633-644. https://doi.org/10.1161/01.RES.0000259563.61091.e8

Perez-Garcia, V., Fineberg, E., Wilson, R., Murray, A., Mazzeo, C. I., Tudor, C., Sienerth, A., White, J. K., Tuck, E., Ryder, E. J., Gleeson, D., Siragher, E., Wardle-Jones, H., Staudt, N., Wali, N., Collins, J., Geyer, S., Busch-Nentwich, E. M., Galli, A., Smith, J. C., Robertson, E., Adams, D. J., Weninger, W. J., Mohun, T., & Hemberger, M. (2018). Placentation defects are highly prevalent in embryonic lethal mouse mutants. *Nature*, *555*(7697), 463-468. https://doi.org/10.1038/nature26002

Posern, G., & Treisman, R. (2006). Actin' together: serum response factor, its cofactors and the link to signal transduction. *Trends Cell Biol*, *16*(11), 588-596. https://doi.org/10.1016/j.tcb.2006.09.008

Rogers, C. D., & Nie, S. (2018). Specifying neural crest cells: From chromatin to morphogens and factors in between. *Wiley Interdiscip Rev Dev Biol*, *7*(5), e322. https://doi.org/10.1002/wdev.322

Saga, Y., Miyagawa-Tomita, S., Takagi, A., Kitajima, S., Miyazaki, J., & Inoue, T. (1999). MesP1 is expressed in the heart precursor cells and required for the formation of a single heart tube. *Development*, *126*(15), 3437-3447. https://www.ncbi.nlm.nih.gov/pubmed/10393122

Shin, C. H., Liu, Z. P., Passier, R., Zhang, C. L., Wang, D. Z., Harris, T. M., Yamagishi, H., Richardson, J. A., Childs, G., & Olson, E. N. (2002). Modulation of cardiac growth and development by HOP, an unusual homeodomain protein. *Cell*, *110*(6), 725-735. https://doi.org/10.1016/s0092-8674(02)00933-9

Smith, E. C., Thon, J. N., Devine, M. T., Lin, S., Schulz, V. P., Guo, Y., Massaro, S. A., Halene, S., Gallagher, P., Italiano, J. E., Jr., & Krause, D. S. (2012). MKL1 and MKL2 play redundant and crucial roles in megakaryocyte maturation and platelet formation. *Blood*, *120*(11), 2317-2329. https://doi.org/10.1182/blood-2012-04-420828

Sun, Q., Chen, G., Streb, J. W., Long, X., Yang, Y., Stoeckert, C. J., Jr., & Miano, J. M. (2006). Defining the mammalian CArGome. *Genome Res*, *16*(2), 197-207. https://doi.org/10.1101/gr.4108706

Sun, Y., Boyd, K., Xu, W., Ma, J., Jackson, C. W., Fu, A., Shillingford, J. M., Robinson, G. W., Hennighausen, L., Hitzler, J. K., Ma, Z., & Morris, S. W. (2006). Acute myeloid leukemia-associated Mkl1 (Mrtf-a) is a key regulator of mammary gland function. *Mol Cell Biol*, *26*(15), 5809-5826. https://doi.org/10.1128/MCB.00024-06

Tallquist, M. D., & Soriano, P. (2000). Epiblast-restricted Cre expression in MORE mice: a tool to distinguish embryonic vs. extra-embryonic gene function. *Genesis*, *26*(2), 113-115. https://doi.org/10.1002/(sici)1526-968x(200002)26:2<113::aid-gene3>3.0.co;2-2

Tallquist, M. D., & Soriano, P. (2003). Cell autonomous requirement for PDGFRalpha in populations of cranial and cardiac neural crest cells. *Development*, *130*(3), 507-518. https://doi.org/10.1242/dev.00241

Trembley, M. A., Velasquez, L. S., de Mesy Bentley, K. L., & Small, E. M. (2015). Myocardin-related transcription factors control the motility of epicardium-derived cells and the maturation of coronary vessels. *Development*, *142*(1), 21-30. https://doi.org/10.1242/dev.116418

Vasudevan, H. N., & Soriano, P. (2014). SRF regulates craniofacial development through selective recruitment of MRTF cofactors by PDGF signaling. *Dev Cell*, *31*(3), 332-344. https://doi.org/10.1016/j.devcel.2014.10.005

Wang, Z., Wang, D. Z., Hockemeyer, D., McAnally, J., Nordheim, A., & Olson, E. N. (2004). Myocardin and ternary complex factors compete for SRF to control smooth muscle gene expression. *Nature*, *428*(6979), 185-189. https://doi.org/10.1038/nature02382

Weinl, C., Wasylyk, C., Garcia Garrido, M., Sothilingam, V., Beck, S. C., Riehle, H., Stritt, C., Roux, M. J., Seeliger, M. W., Wasylyk, B., & Nordheim, A. (2014). Elk3 deficiency causes transient impairment in post-natal retinal vascular development and formation of tortuous arteries in adult murine retinae. *PLoS One*, *9*(9), e107048. https://doi.org/10.1371/journal.pone.0107048

Xie, Z., Bailey, A., Kuleshov, M. V., Clarke, D. J. B., Evangelista, J. E., Jenkins, S. L., Lachmann, A., Wojciechowicz, M. L., Kropiwnicki, E., Jagodnik, K. M., Jeon, M., & Ma'ayan, A. (2021). Gene Set Knowledge Discovery with Enrichr. *Curr Protoc*, *1*(3), e90. https://doi.org/10.1002/cpz1.90

Zaromytidou, A. I., Miralles, F., & Treisman, R. (2006). MAL and ternary complex factor use different mechanisms to contact a common surface on the serum response factor DNA-binding domain. *Mol Cell Biol*, *26*(11), 4134-4148. https://doi.org/10.1128/MCB.01902-05